Structure of mitoribosome reveals mechanism of mRNA binding, tRNA interactions with L1 stalk, roles of cofactors and rRNA modifications

Vivek Singh[1,13], Yuzuru Itoh[1,2,13], Samuel Del'Olio[3,13], Asem Hassan[4,5,13], Andreas Naschberger[1,6], Rasmus Kock Flygaard[7], Yuko Nobe[8], Keiichi Izumikawa[9], Shintaro Aibara[1], Juni Andréll[10], Paul C Whitford[4,5], Antoni Barrientos[3,11,12], Masato Taoka[8], Alexey Amunts[1*]

[1] Science for Life Laboratory, Department of Biochemistry and Biophysics, Stockholm University, 17165 Solna, Sweden.
[2] Department of Biological Sciences, Graduate School of Science, University of Tokyo, 113-0033 Tokyo, Japan.
[3] Department of Molecular and Cellular Pharmacology, University of Miami Miller School of Medicine, Miami, FL 33136, United States.
[4] Department of Physics, Northeastern University, Boston, MA, 02115, United States.
[5] Center for Theoretical Biological Physics, Northeastern University, Boston, MA, 02115, United States.
[6] King Abdullah University of Science and Technology, Thuwal 23955, Saudi Arabia.
[7] Department of Molecular Biology and Genetics, Danish Research Institute of Translational Neuroscience - DANDRITE, Nordic EMBL Partnership for Molecular Medicine, Aarhus University, 8000 Aarhus C, Denmark.
[8] Department of Chemistry, Graduate School of Science, Tokyo Metropolitan University, Minami-osawa 1-1, Hachioji-shi, Tokyo 192-0397, Japan.
[9] Department of Biotechnology, Global innovation research institute, Tokyo University of Agriculture and Technology, Saiwai-cho 3-5-8, Fuchu-shi, Tokyo 183-8509, Japan.
[10] Department of Medical Biochemistry and Biophysics, Karolinska Institutet, 17177, Stockholm, Sweden.
[11] Department of Neurology, University of Miami Miller School of Medicine, Miami, FL 33136, United States.
[12] Department of Biochemistry and Molecular Biology, University of Miami Miller School of Medicine, Miami, FL 33136, United States.
[13] These authors contributed equally

* correspondence: amunts@scilifelab.se

The mitoribosome translates mitochondrial mRNAs and regulates energy conversion that is a signature of aerobic life forms. We present a 2.2 Å resolution structure of human mitoribosome together with validated mitoribosomal RNA (rRNA) modifications, including aminoacylated CP-tRNA^{Val}. The structure shows how mitoribosomal proteins stabilise binding of mRNA and tRNA helping to align it in the decoding center, whereas the GDP-bound mS29 stabilizes intersubunit communication. Comparison between different states, with respect to tRNA position, allowed to characterize a non-canonical L1 stalk, and molecular dynamics simulations revealed how it facilitates tRNA transition in a way that does not require interactions with rRNA. We also report functionally important polyamines that are depleted when cells are subjected to an antibiotic treatment. The structural, biochemical, and computational data illuminate the principal functional components of the translation mechanism in mitochondria and provide the most complete description so far of the structure and function of the human mitoribosome.

The human mitoribosome translates at least 13 respiratory chain protein-coding mRNAs from the mitochondrial genome [1]. It consists of three rRNAs and at least 82 mitoribosomal proteins, 36 of which have no corresponding homologs in bacterial and cytosolic ribosomes. The mitochondrial rRNA is reduced compared to its bacterial counterpart (2,512 vs 4,568 nucleotides in *Escherichia coli*), $tRNA^{Val}$ has been incorporated as an additional constituent, and protein components are extended (~18,075 vs 7,536 residues in *E. coli*) [2]. The mitoribosomal proteins might have functional roles in mitochondria-specific aspects of translation, and therefore mutations in the corresponding genes result in cardio- and encephalomyopathies [3, 4]. However, due to the limited resolution and heterogeneity of the characterized complexes, the available models are currently incomplete, and many mitoribosomal protein key elements are described as unassigned densities [5, 6, 7, 8, 9, 10]. The existing models suggest that mitoribosomal proteins might play a role in binding mRNA, regulatory elements such as the L1 stalk are probably remodeled, and the specific mitoribosomal protein mS29, a putative GTPase is associated with inter-subunit communication. Yet, the lack of experimental data leaves open the questions of a functional involvement.

The mitochondrial rRNA is modified, and dedicated post-transcriptionally activated enzymes provide means for the regulation of gene expression and mitoribosome assembly [11]. Due to the central role of the human mitoribosome in cellular energy production, defects in rRNA modification result in fatal clinical syndromes from birth [12, 13]. Some of the bacterial counterpart modifying enzymes are missing from mitochondria, for example methyltransferases RlmA, RlmB, RmsE and pseudouridine synthase RluA, while other mitochondria-specific ones have evolved [14]. Therefore, rRNA modifications are different, and they have been identified by various experimental approaches [11, 15, 16, 17, 18, 19, 20, 21, 22, 23], furthermore recent structural studies visualized individual rRNA modifications on the mitoribosomal large (LSU) [24] and small (SSU) subunits [25, 26]. However, the entire set of modifications is yet to be quantitatively identified and visualized in the presence of bound ligands in order to enable a detailed examination of their roles. To date, the molecular mechanisms compensating for the lack of bacteria-like modifications remain unknown, as well as the modifications and the amino-acylation state of the structural $tRNA^{Val}$.

Mitoribosomes are also linked to age-related diseases that are associated with decline in mitochondrial function and biogenesis [27, 28, 29, 30]. Aging-related pathological changes can be inhibited by polyamine consumption [31, 32], which also has anti-inflammatory effects in mouse models *in vivo* [33]. Polyamines have been shown to be essential for mammalian cell differentiation and proliferation through their impact on translation dynamics [34, 35]. However, no polyamine biosynthetic pathways within mitochondria have been found, and their role in mitochondrial physiology remained unknown. Whether mitoribosomes might be related to these phenomena and associated with cellular senescence via polyamines needs to be explored.

To address these issues, we combined high resolution structural studies of mitoribosomal complexes with mass spectrometry based quantitative RNA analysis, biochemistry, and molecular dynamics simulations.

111 **Structure determination**

112 To produce a 2.2 Å overall resolution map of the mitoribosome, we collected five separate cryo-
113 EM datasets. Selected monosome particles were subjected to per-particle defocus, beam-tilt and
114 per-particle astigmatism correction, followed by Bayesian polishing [36, 37]. The data was then
115 sorted into 86 optics groups based on acquisition areas followed by beam-tilt, magnification
116 anisotropy and higher order aberration correction [38]. A final set of 509,691 particles yielded a 2.2
117 Å map. The local resolution was further improved by performing masked refinements around
118 different regions of the monosome. In addition, we obtained a 2.6 Å resolution map in the
119 presence of mRNA and three tRNAs in the classical state, and 3.0 Å resolution map with two
120 tRNAs in the hybrid state (Supplementary Figs. 1 and 2). The improved resolution allowed
121 building the most complete available model of the mitoribosome, including several key protein
122 extensions involved in tRNA binding (Fig. 1a). The presence of mRNA on the mitoribosome
123 further enabled modeling 32 of its residues, which we then used to trace mitochondria-specific
124 elements involved in mRNA binding and put the rRNA modifications in a functional context
125 (Fig. 1b).
126 To provide a description of the conformational changes associated with tRNA movement, we
127 next focused efforts on modelling the L1 stalk. Thus, we merged particles containing tRNA in
128 the E-site and through partial signal subtraction [39] and obtained a 2.9 Å resolution map of the
129 region, enabling model building of the L1 stalk (Supplementary Fig. 1). We then used this model
130 to perform molecular simulations of the complete ribosome with tRNAs.

131

132 **rRNA and protein modifications, aminoacylated tRNA^{Val}, polyamines**

133 On the rRNA level, the quality of the map allowed the modeling of 13 rRNA modifications, of
134 which 6 are mitochondria specific compared to *E. coli* [21]. All the rRNA modifications
135 were validated by a tailored quantitative method of Stable Isotope-Labeled riboNucleic Acid as
136 an internal Standard (SILNAS) [40] (Supplementary Figs. 3,4). The mitochondria specific
137 modifications include base methylations m^{5}U1076, m^{5}C1488 in the SSU; m^{1}A2617 in the LSU;
138 and m^{1}A9, m^{2}G10 and ψ39 in the tRNA^{Val} incorporated in the central protuberance (CP) [41, 42, 43]
139 (Fig. 1b). In the map, methylations of rRNA were identified by systematically examining the
140 density map for the presence of unmodeled densities continuous with the base or sugar moieties
141 of rRNA residues (Fig. 2). Identity of the two high-occupancy pseudo-uridines was established
142 based on the presence of a structured water molecule within hydrogen-bonding distance from the
143 N5 atom.

144 The tRNA^{Val} modifications are consistent with the previous mass-spectrometry data on isolated
145 mitochondrial tRNAs from a general pool [44] (Fig. 3). The density further revealed that the
146 tRNA^{Val} incorporated in the CP is amino acylated (Fig. 2a). In the structure, ψ39 of tRNA^{Val}
147 contributes to the conformation of the anticodon arm, which contacts uL18m, mL38, mL40 and
148 mL48 (Fig. 3a). In addition, two methylated residues, m^{1}A and m^{2}G, are observed at the
149 positions 9 and 10, respectively in the D arm (Fig. 3a). m^{1}A9 is stacked between G45 and A46

150 and forms a base triple with the second base pair (C11:G24) of the D stem. On the other hand,
151 m^2G10 is stacked between C11 and A26 and forms the first base pair (m^2G10:C25) of the stem,
152 which further interacts with G45 to be a base triple. These methylations facilitate the stacking
153 and hydrogen bonds among bases, and thereby contribute to the conformation of the D arm,
154 which contacts uL18m and mL38 (Fig. 3a-c). The terminal A76 has a base-specific interaction
155 with Q175 of mL46 and together with Valine is stacked with F165 and F215 (Fig. 3d).
156 A notable feature of the cryo-EM map is the presence of continuous tubular densities associated
157 with rRNA that we assigned as polyamines, justified by the electrostatic and hydrogen-bonding
158 interactions at the amine groups (Supplementary Fig. 5). Thus, in addition to a previously
159 assigned spermine (SPM) [45], we detected one triamine spermidine (SPD) in the SSU, and a
160 diamine putrescine (PUT) and three SPDs in the LSU. The identified polyamines are bound to
161 negatively charged rRNA where mitochondria specific changes occur, providing required
162 structural support (Fig. 4; Supplementary Fig. 5). For example, SPD3301 in the LSU fills the
163 formed space of a shortened mitoribosomal protein uL2m, which has undergone reduction in the
164 human mitoribosome. SPD3303 is tethered to uL3m, where a bacterial counterpart has a
165 signature Q150 methylation, therefore replacing the post-translational modification. The PUT is
166 found in the exit tunnel upper region of uL22m hairpin.

167 Finally, the model contains six protein modifications; three iron-sulfur clusters, one of which is
168 coordinated by uL10m and mL66 and reported here for the first time, and a molecule of
169 nicotinamide adenosine dinucleotide (NAD) reported previously [26, 45, 46] (Fig. 1b, Supplementary
170 Table 1). We also identified a disulfide bond in one of the two redox active cysteine pairs in
171 mS37 (CHCHD1) (Fig. 2) that is oxidized in the intermembrane space during mitochondrial
172 import, representing a quality control mechanism [47].

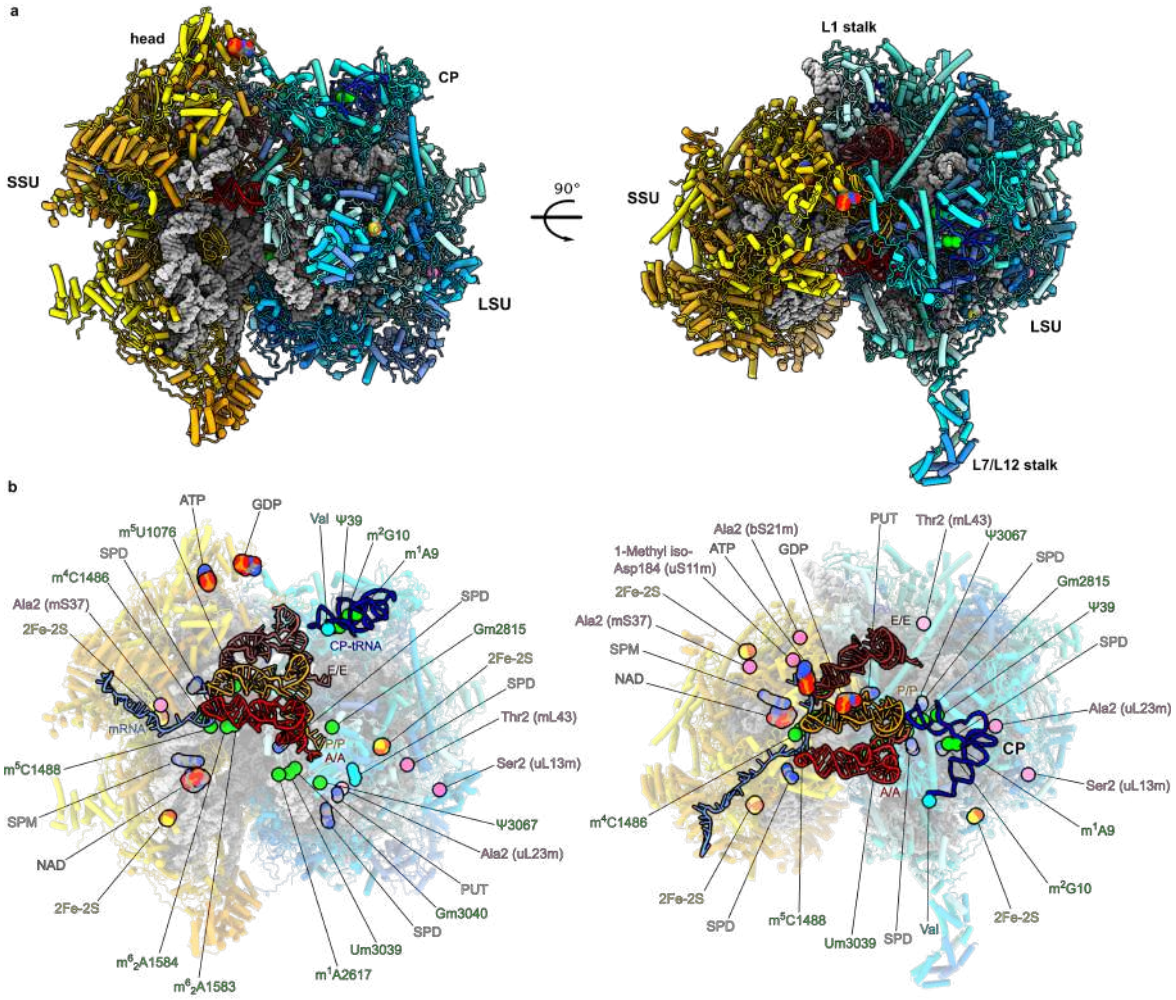

Fig. 1: Structure of the human mitoribosome. a, Overview of the 2.2 Å resolution model with mRNA and tRNAs. Proteins are shown as cartoons colored in blue for the LSU and yellow for the SSU. The rRNA is shown as grey surface. Newly identified features are shown as spheres. **b,** The newly identified cofactors and modifications are indicated against background of translucent rRNA and proteins with tRNAs and mRNA shown in cartoon. We observe 13 rRNA modifications (green), 6 protein modifications (pink), 3 iron-sulfur clusters (red-yellow), guanosine diphosphate (GDP), adenosine triphosphate (ATP), NAD, SPM, 4 SPDs and PUT.

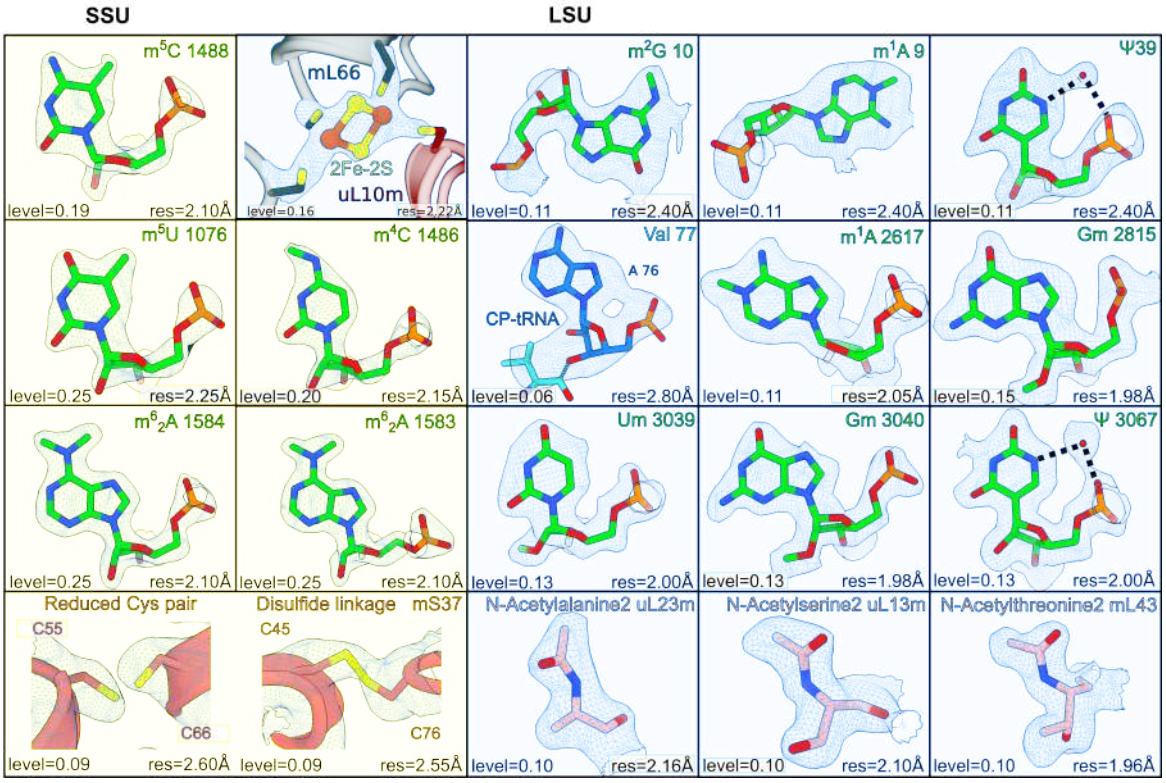

Fig. 2: High resolution features. Modified rRNA residues and disulfide-linked or reduced cysteine residues of mS37 in the SSU (yellow background). Modified rRNA and protein residues, and 2Fe-2S cluster in the LSU (cyan background). Their corresponding densities in the 2.2 Å map are shown as mesh at indicated threshold (bottom left) and local resolution (bottom right) levels.

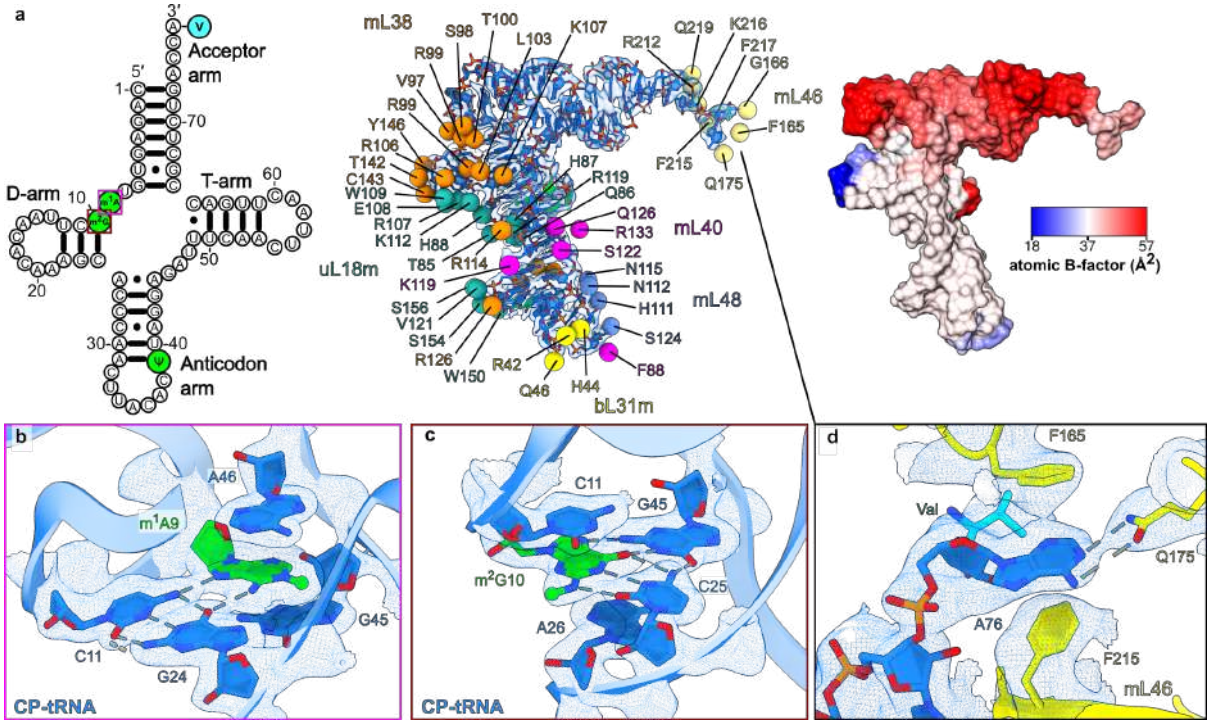

Fig. 3: Interactions and post-transcriptional modifications in CP-tRNA of the mitoribosome. a, CP-tRNA^{Val} (left to right) secondary structure diagram with modified nucleotides (green) and valine (cyan) highlighted, protein-contact map, *B*-factor representation. **b,c,** Interactions of the modified m^{1}A9 and m^{2}G10 nucleotides of CP-tRNA^{Val}. **d,** Interactions of A76 and V77 of CP-tRNA^{Val} with mL46. The cryo-EM density map is displayed for panels b-d (consensus map) as blue mesh. Panels (b) and (c) are related to panel (a) on the left by colored boxes.

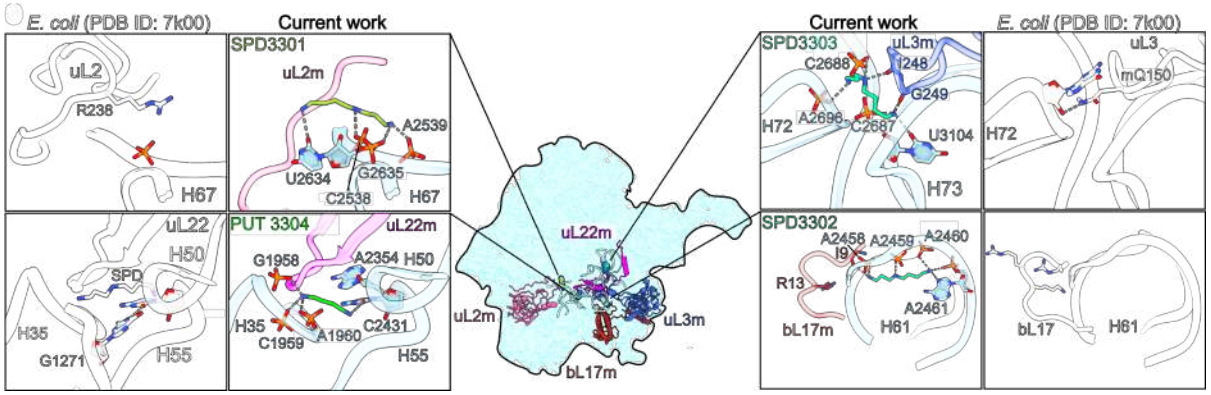

Fig. 4: Polyamines functionally compensate for rRNA and protein alterations. Central inset shows positions of polyamines and interacting rRNA and proteins in the LSU. For each polyamine, its environment and interacting partners are shown in zoom-in panels with *E. coli* counterparts [48] (white) for comparison.

201 **Initial binding of mRNA involves Y-N-C-Y motif coevolved with mS39**

202 The modulation of a stable mitoribosomal complex allowed us to resolve the mRNA path and
203 investigate mitoribosome-specific components involved in mRNA recognition (Fig. 5,
204 Supplementary Fig. 6, Supplementary Video 1). It engages seven helical repeats of mS39 with
205 specific contacts within a prominent positively charged groove (Fig. 5a). Particularly, a
206 pyrimidine ring of the mRNA nucleotide in position 25 is stacked between H489 and R524 and
207 interacts with S490 of mS39 (Fig. 5a,b). Hydrogen bonding between the side chain of R377 of
208 mS39 and nucleotide 27 favors cytosine over uracil because the protonated N3 of a uracil would
209 partially clash with the protonated Nη of R377. R343 of mS39 forms a hydrogen bond with the
210 pyrimidine ring of nucleotide 28. Thus, the structure reveals a binding motif: 25 pyrimidine (Y),
211 27 cytosine (C), 28 pyrimidine (Y) (Fig. 5a,b). Bioinformatic analysis showed that the Y-N-C-Y
212 motif is enriched in mitochondria and distributed over the entire length of each of the 12 open
213 reading frames in the guanine-rich heavy DNA strand, suggesting a co-evolution of the
214 mitochondrial DNA and the mitoribosome (Fig. 5c, Supplementary Fig. 7). The only mammalian
215 protein-coding gene with a reduced frequency of the Y-N-C-Y motif is the *MT-ND6* that is on
216 the light strand and codes for an 18-kDa subunit of complex I. The expression of the ND6
217 mRNA is unique, as it requires an auxiliary factor FASTK to generate the mature form,
218 suggesting a dedicated regulatory mechanism [49].

219 The most 5' contact between mRNA and mS39 is ~50 Å from the channel entrance, and by
220 following the mRNA density toward the decoding center, we identified six specific
221 mitoribosomal proteins that are important for mRNA recruitment, channel opening, and precise
222 alignment of the message for translation in the decoding center. In our structure, the Y-N-C-Y
223 motif forms a ~100° turn (kink-1) in the mRNA midway through mS39 (Fig. 5a and
224 Supplementary Video 1). After the kink, the N-terminal mitochondria-specific extension of
225 uS5m supports the path of mRNA over a distance of ~60 Å, involving a unique N-terminal
226 polybasic stretch of 14 residues 111-124 (KKGRGKRTKKKKRK) together with R237 and
227 K239 (Fig. 5d, Supplementary Video 1, Supplementary Fig. 6). From the side of the SSU head,
228 mS35 provides potential stabilizing electrostatic interactions to mRNA with N-terminal residues
229 K46 and K49 (Fig. 5e,f). This mitochondria-specific extension of uS5m structurally replaces
230 bacterial bS4 and uS3-CTD that interact with mRNA (Supplementary Fig. 6) and confer RNA
231 helicase activity on the bacterial ribosome [50]. Just before the channel entry, the binding of
232 mRNA induces a conformational change of the N-terminal extension of uS9m that contacts the
233 mRNA nucleotide at position 15 via the backbone of V55 (Fig. 5e,g; Supplementary Video 1),
234 which in the absence of mRNA blocks the entrance to the decoding center [51]. Thus, uS9m exists
235 in a closed conformation in the absence of mRNA, and upon mRNA threading, a conformational
236 change in uS9m allows the passage (Fig 5h).

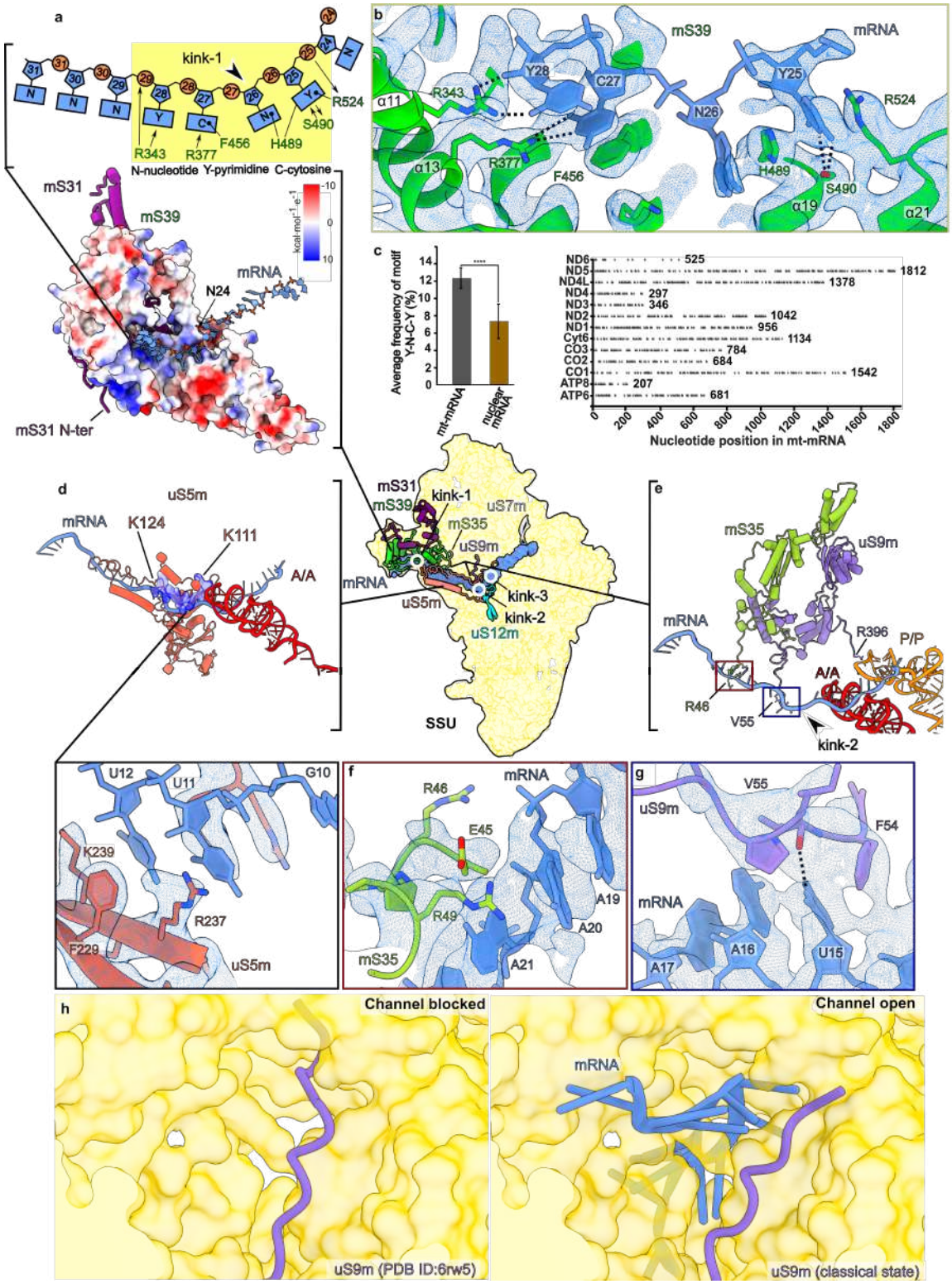

Fig. 5: Specific protein elements involved in mRNA binding.

239 **a,** Electrostatic coulomb potential surface representation of the model shows a positively charged
240 groove (blue) on mS39 that accommodates the mRNA. N-terminal loop of mS31 interacts with
241 mS39. Y-N-C-Y motif and its interactions with mS39 residues are depicted as a schematic.
242 Position of kink-2 is marked. **b,** Interactions of the Y-N-C-Y motif with mS39 and density map
243 (mesh). Protein mS31 has been removed for clarity. **c,** Average percentage frequency of Y-N-C-
244 Y motif (left) with +/- standard deviation for mitochondrial mRNAs (excluding ND6; dark grey
245 bar) and nuclear mRNA (brown bar). P-value (<0.0001) calculated by Welch's unpaired t-test.
246 Positions of the Y-N-C-Y motif in the mt-mRNAs are shown as discs (right) to depict its
247 distribution along the mt-mRNA sequences. The total number of residues for each mt-mRNA is
248 indicated. **d,** Overview of uS5m showing a region of contact with mRNA. The polybasic stretch
249 111-124 along the mRNA is colored by electrostatic potential. Interacting residues between
250 uS5m and mRNA are shown with the local density map. **e,** Interactions of mS35 and uS9m with
251 mRNA at the channel entry and the P-site. **f,** R46 and R48 of mS35 potentially interact with the
252 mRNA backbone, and the density suggests flexibility of the side-chains. **g,** uS9m forms stacking
253 and hydrogen bonding interactions with mRNA position 15 via F54 and V55, respectively. **h,**
254 uS9m N-terminus (purple cartoon) adopts alternative conformations that result in mRNA channel
255 blocked or open states regulating mRNA access to the SSU (gold surface).
256
257 **mL40 N-terminal tail stabilizes the A- and P-site tRNAs and decoding interactions**

258 We then examined the role of mitoribosomal proteins in the mRNA alignment. The structure
259 shows that to enter the SSU channel, the mRNA must be kinked again (kink-2), and in the A-site
260 the nucleotide at position 9 is stabilized by uS12m (Supplementary Fig. 8). Here, a conserved
261 K72 side chain forms a salt bridge with the phosphate of nucleotide 9 (last nucleotide in the A-
262 site codon). At the same time, *cis*-proline P73 (Supplementary Fig. 8) coordinates two potassium
263 ions, one of which directly coordinates 2´O of nucleotide 9 (Supplementary Fig. 8,
264 Supplementary Video 1) and stabilizes the decoding center. The densities identified as two
265 potassium ions have been observed previously, but modeled as Mg^{2+} (PDB 4V51) [52] or waters
266 (PDB 7K00) [48, 52]. However, they have been experimentally identified as K^{+} by long wavelength
267 X-ray diffraction analysis (PDB 6QNR) [53], which agrees with our assignment (Supplementary
268 Fig. 8).

269 Next, between the A- and P-site, the map reveals a third kink in the mRNA (kink-3), which is co-
270 localized with a 35-Å long density extending from the CP in between the two tRNAs (Fig. 6a,
271 Supplementary Fig. 9a) that could not be previously interpreted. We identified it as a positively
272 charged N-terminus of mL40 with the terminal backbone amino group of S47 forming a salt
273 bridge with the backbone phosphate of the mRNA at position 7 in the A-site (Fig. 6a,
274 Supplementary Fig. 9b), and the interaction is further stabilized via a magnesium ion coordinated
275 by the phosphate of G1485. In addition, the hydroxyl group of S47 interacts with the mRNA
276 nucleotide base at position 6 in the P-site (Fig. 6a, Supplementary Video 1), although the
277 contacts are likely to be flexible. Moreover, the base orientation allows any nucleotide to interact
278 with S47 (Supplementary Fig. 9c). The concept is analogous to the cytosolic ribosome that

engages uS19 for tRNA stabilization and mRNA interactions in the decoding center [54] (Fig. 6b). The presence of four lysine residues 52-55 (Fig. 6a, Supplementary Fig. 9b), might suggest that mL40 contributes to balancing the charge between the A- and P-tRNAs. Together with R51, which forms salt bridges with A1560 and C1561 in h44, the positively charged patch compensates for the negative RNA charges accumulated in that region (Fig. 6a, Supplementary Fig. 9b, Supplementary Video 1). Further in the P-site, we observe a well-resolved density showing the conserved C-terminal R396 of uS9m interacting with the anticodon loop of the P-site tRNA (Supplementary Fig. 9d). Finally, in the E-site, uS7m residues G164-165 further contribute to mRNA stabilization (Supplementary Fig. 9e). Thus, mitoribosomal proteins play a role in mRNA binding.

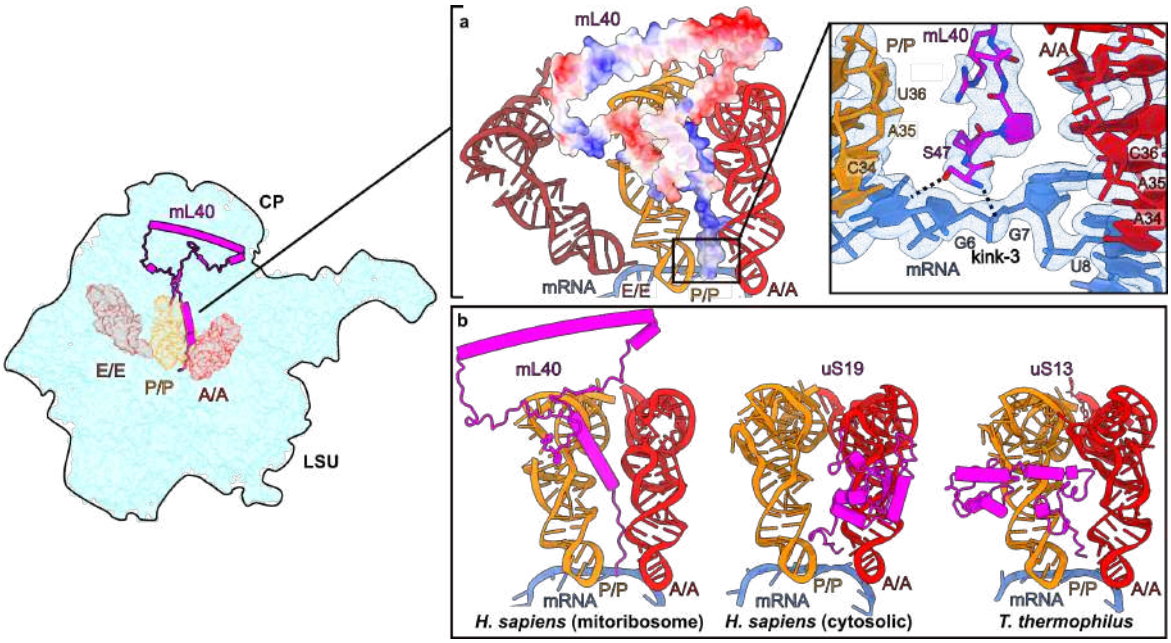

Fig. 6: Analysis of mRNA binding in tRNA sites. a, Interactions of mL40 (shown with electrostatic potential of the model) with mRNA between A/A- and P/P-tRNAs. Hydrogen bonds G6 base and G7 phosphate are shown as dashed lines. **b,** Comparison of mL40-tRNA interaction (left) with those of uS19 (middle) and uS13 (right) in human cytosolic [54] and *T. thermophilus* ribosome [52], respectively.

mRNA alignment in the decoding center and rRNA modifications

In the decoding center, the universally conserved G902 is in *anti* conformation, while A1557 and A1558 are flipped out from h44 to interact with the A-site codon:anti-codon helix in the canonical manner [55, 56] (Supplementary Fig. 10). A well-resolved density, combined with the mass-spectrometry SILNAS [40, 57, 58] approach further allowed us to validate the complete set of the rRNA modifications, including six mitochondria specific, and propose a role in stabilizing the decoding center (Fig. 5, Supplementary Figs. 4 and 5). Close to the decoding center, the residue G899 was recently shown to interact with streptomycin in human mtSSU [45]. Its

methylated to m^7G527 in *E.coli* (Supplementary Fig. 10) and this modification partly contributes to streptomycin sensitivity [59]. In the P-site, two base-methylated nucleotides m^4C1486 and m^5C1488 flank the base triple C1487:A1564:U1563 by stabilizing the stacking interactions (Fig. 5a,b). The orientation of N^4-methylated m^4C1486 towards mRNA is conserved with respect to *E. coli*, where the corresponding residue is also 2'-O methylated ($m^4Cm1402$) (Supplementary Fig. 10). m^4C1486 together with C1487 interacts with the phosphate group of the last nucleotide in the P-site mRNA codon via hydrogen bonds (Fig. 5a,b). Further, phosphate group of m^4C1486 coordinates a magnesium ion, which stabilizes a conserved kink of the mRNA between A- and P-sites (Fig. 7a). In contrast to the *E. coli* P-site, U1563 does not have an N^3-methylation (m^3U1498 in *E. coli*) (Supplementary Fig. 10). This lack of N^3-methylation allows U1563 together with C1487 to form a water mediated interaction with the P-site codon (Fig. 7a,b). Further, the conserved dimethylated residues, $m^6{}_2A1583$ and $m^6{}_2A1584$ orient the nucleotide U1563 such that the ribose of U1563 forms a hydrogen bond to a phosphate group of the second nucleotide in the P-site mRNA codon, while the phosphate of U1563 forms a hydrogen bond with the ribose on the first codon nucleotide (Fig. 7b). The two dimethylated nucleotides facilitate A1080 positioning for the 2′-OH to hydrogen bond with N3 of m^5U1076. This together with methylation of m^5U1076 contributes to the stability of h24 loop that interacts with the P-tRNA anticodon stem at position 38 via A1078 (Fig. 7a,b).

In the A-loop of H92, there are two 2′-O-methyl modified nucleotides Um3039 and Gm3040. The 2′-O-methyl of Um3039 sterically positions the bases of Gm3040 and U3041 to form interactions with the nucleotides C75 and C74 of the A-tRNA, respectively (Fig. 7c,d). The 2′-O-methyl of Gm3040 present in the cytosolic but not bacterial ribosome and interacts with the base of A3069 to stabilize the conformation of Gm3040. Furthermore, the bacterial counterpart rRNA that interacts with A-tRNA (C75) is G:C, whereas in our structure it's A:U (3069:2994) that is less stable, and thus stabilized by the mitochondria-specific methylation of Gm3040 and base-pairing interactions with ψ3067 (Fig. 7d). In the LSU, mitochondria-specific m^1A2617 positions U2614 into a wedged interaction (Fig. 7e). Surprisingly, there is only weak sugar puckering for m^1A2617 (Fig. 2a). It bears a partial positive charge at N1 and interacts with U2649 of H61. The interactions mediated by m^1A2617 potentially contribute to the structuring of H71 loop that participates in an intersubunit bridge shares an interface with the A-loop (Fig. 7e). The universally conserved Gm2815 in the P-loop forms Watson-Crick base pairing with C75 of P/P-tRNA, similar to the interactions of Gm3040 of the A-loop (Fig. 7f).

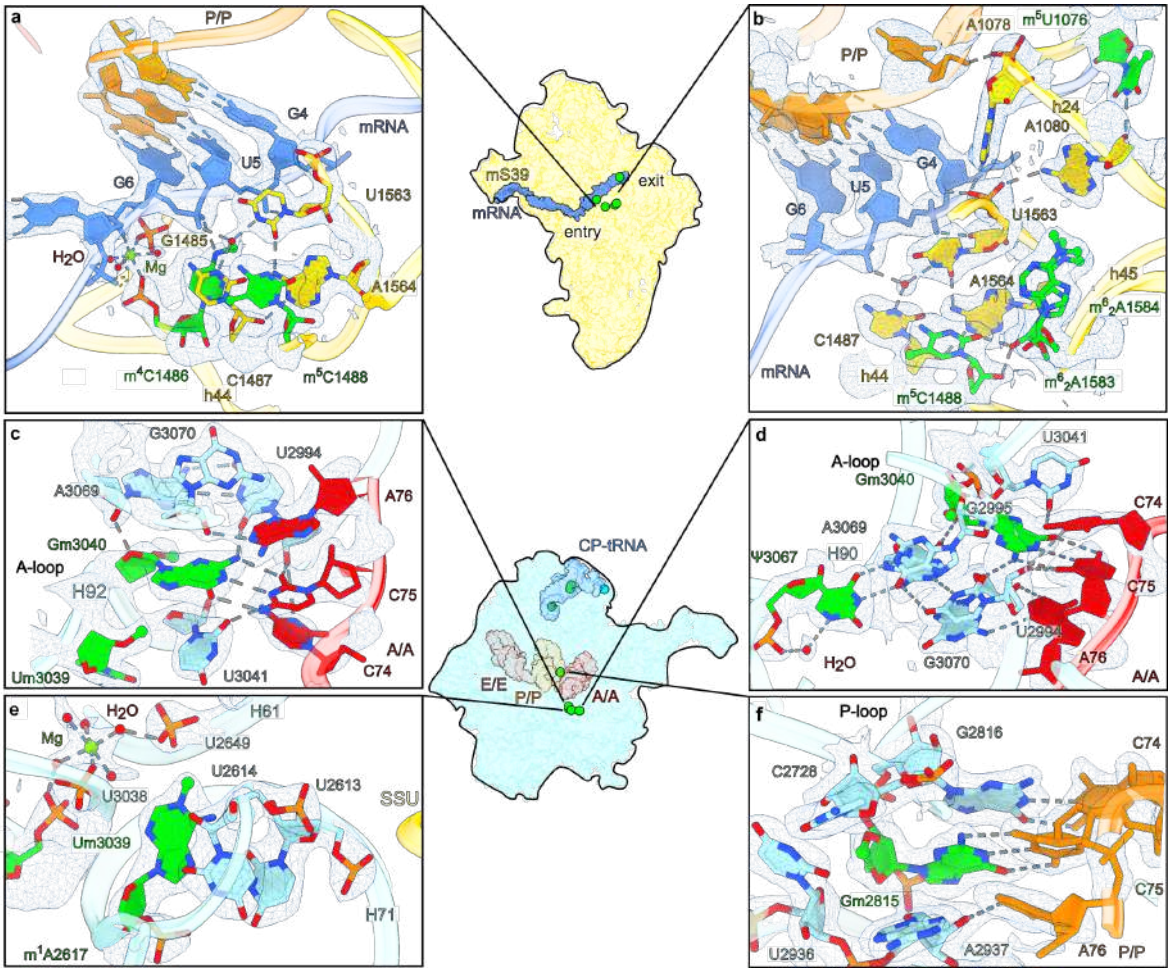

Fig. 7: Post-transcriptional modifications in functional centers of the mitoribosome. **a,** Base-methylated m^4C1486 and m^5C1488 and the interactions at the P-site mRNA codon. **b,** The dimethylated $m^6{}_2A1583$, $m^6{}_2A1584$ and base-methylated m^51076 facilitate interactions with mRNA codon and P-tRNA. **c,** 2′-*O*-methyl modified Um3039 and Gm3040 lead to interactions with A-tRNA. **d,** Gm3040 and Ψ3067 contribute to the interface with the A-tRNA. **e,** m^1A2617 contributes to a stabilization of inter-subunit bridge and the A-loop. **f,** Gm2815 base-pairs with P-tRNA. Cryo-EM density map (A/A P/P E/E state) is displayed as a blue mesh.

Structure of the mitoribosomal L1 stalk reveals its unique protein features

To investigate whether mitoribosomal proteins might also have influence on tRNA rearrangement in the E-site, we aimed to perform molecular simulations of the mitochondrial L1 stalk. Therefore, we modeled the complete structure of the L1 stalk, which relies on mitochondria specific protein elements. In the structure, the E-tRNA is stabilized via mitochondria-specific protein elements of the C-terminal domain of uL9m and 33-residue N-terminal extension of uL1m (Fig. 8a,b). The orientation of the uL9m C-terminal domain adopts a

352 previously unseen folded conformation involving a ~75° rotation towards the E-tRNA (Fig. 8c).
353 This unexpected conformational difference is facilitated by the C-terminal helix in the extension
354 that reaches and contacts the non-base-pairing part and the distal short hairpin of the rRNA H76
355 (Fig. 8d). The resulting projection of uL9m towards the ribosomal core reduces the distance
356 between the central helix and the C-terminus of uL1m from ~70 to only ~30 Å. This distance is
357 spanned by the uL1m mitochondria-specific extension that forms direct contacts with the central
358 helix of uL9m (Fig. 8d-f). Therefore, our model of the L1 stalk establishes a tertiary
359 mitoribosomal complex uL9m:uL1m:rRNA-H76, where uL9m acquires a new functional role.
360 From the opposite side, the mitochondria-specific mL64 approaches the T-arm through its long
361 C-terminal helix extending to the tRNA binding sites.

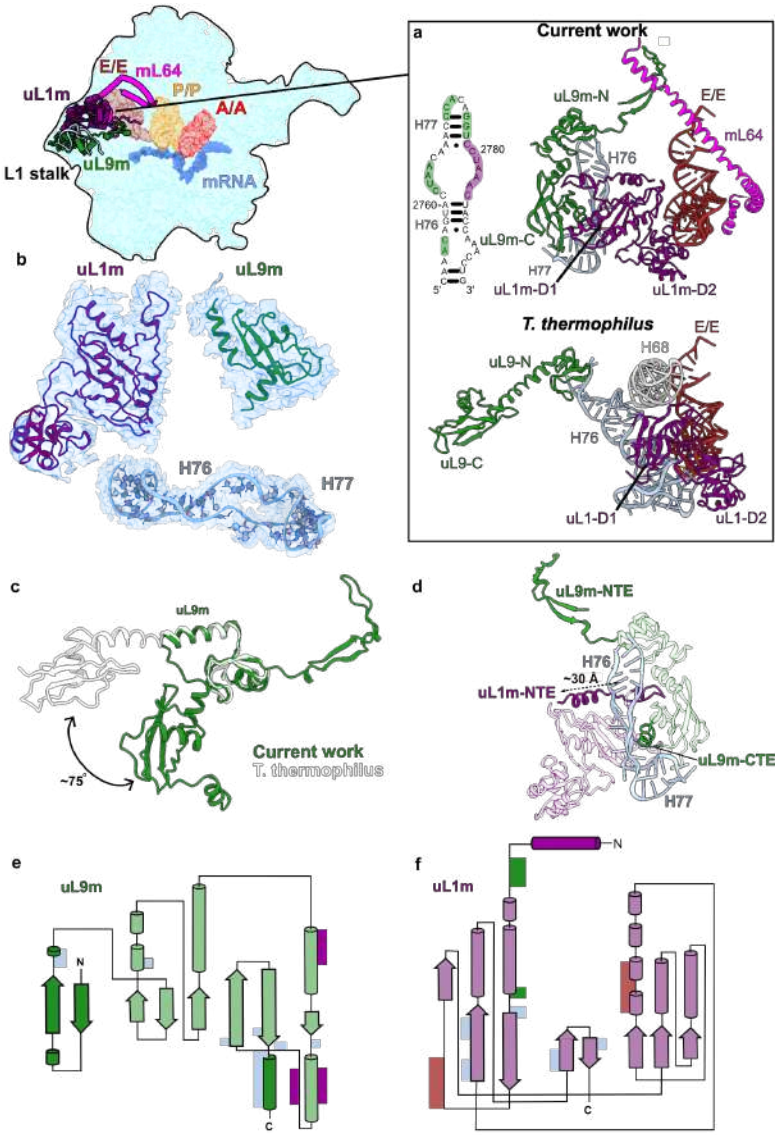

362
363 **Fig. 8: Structural features of the L1 stalk and interactions with tRNA.**

364 **a,** The L1 stalk components uL9m (green), uL1m (purple) rRNA helix H76-77 (residues 2757-
365 2790, light blue), as well as mL64 (magenta) interact with E/E-tRNA. The structure and
366 interactions are different from *T. thermophilus* (PDB ID: 4V51) [52] **b,** Components of the L1 stalk
367 modeled into their respective densities (shown as mesh). **c,** Comparison of uL9m conformation
368 with that of *T. thermophilus* uL9 (white PDB ID 4V51). **d,** Model of uL1m stalk with uL9m in
369 green and uL1m in purple, highlighting mitochondria-specific protein elements. **e,** 2D diagram of
370 uL9m showing interactions with E/E-tRNA (brown bars), rRNA (light-blue bars), uL1m (dark-
371 blue bars). Conserved regions are shown in light and mitochondria-specific in dark colors. **f,** 2D
372 diagram of uL1m color-coded as in panel d.
373

374 **Recognition of tRNA by the L1 stalk and intersubunit communication**

375 We next used an all-atom structure-based model [60, 61] to simulate hundreds of transitions of the
376 tRNA from the P site to P/E state (Fig. 9a,b; Supplementary Video 2). To isolate the influence of
377 uL1m and mL64, we compared the dynamics with four variants of the model (Fig. 9c; see
378 Methods): 1) baseline model; 2) truncated mL64 (ΔmL64) with C-terminal region starting with
379 Q112 being removed to prevent steric interactions between mL64 and EE-tRNA without
380 disturbing the rest of the protein.; 3) modified uL1m (ΔuL1m) where stabilizing interactions
381 between uL1m and P-site-tRNA are scaled down compared to the baseline model (values
382 available in methods); 4) both ΔmL64 and ΔuL1m modifications are included (see methods
383 section for details of the models). Using these models, we simulated 1066 spontaneous (non-
384 targeted) transitions between the classical (A/A P/P) and hybrid (A/P P/E) states, which include a
385 ~40 Å displacement of the P-tRNA and spontaneous rotation of the SSU (Supplementary Video
386 2). A mechanistic insight from these calculations is that mL64 imposes strict limits on the
387 pathways that are accessible to tRNA, which thereby favors a specific sequence of
388 conformational substeps during P/E formation (Fig. 9d-g). As a result, mL64 ensures that the
389 tRNA is properly positioned and may reliably engage uL1m as the tRNA approaches the E site.
390 The structure also shows that due to the different type of tRNA binding, no base pairs are formed
391 between the E/E-tRNA and mRNA, unlike those found in bacteria [62] (Supplementary Fig. 9e).
392 Instead, the protein uS7m undergoes a conformational change in which residues G164-165
393 directly contact the mRNA and stabilize its binding (Supplementary Fig. 9e, Supplementary
394 Video 1). Thus, upon each translation step, a tRNA is recognized in the E-site and escorted from
395 the mitoribosome without involving rRNA, which is strikingly different from bacterial and
396 cytosolic counterparts.

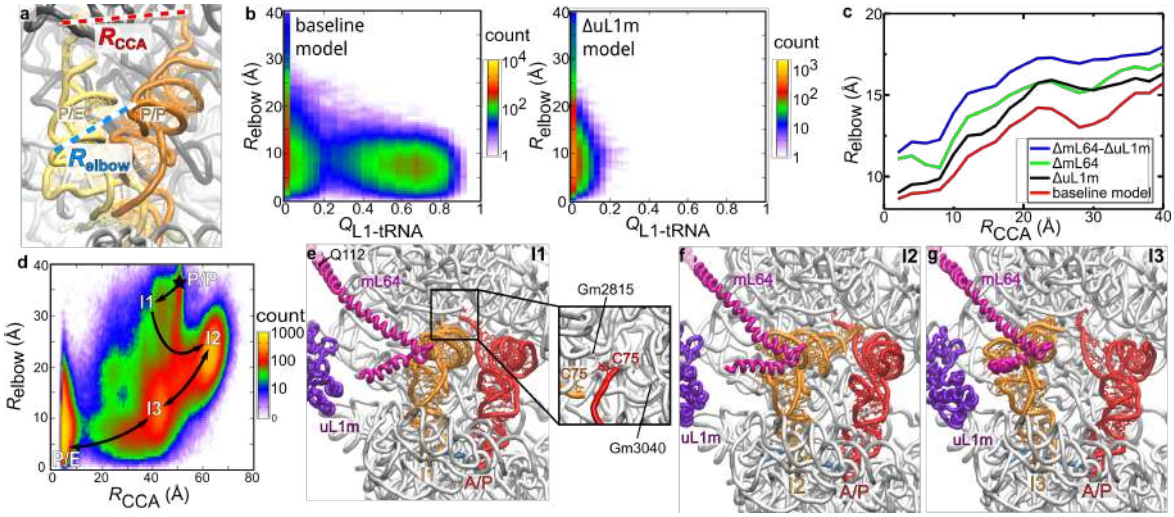

Fig. 9: Simulations of P/E formation reveal the influence of mitochondria-specific proteins. **a,** Distances R_{elbow} and R_{CCA} are used to describe the position of the tRNA during P/E formation. **b,** Probability distribution as a function of P-site tRNA elbow position (R_{elbow}) and the fraction of uL1m-tRNA contacts ($Q_{L1\text{-}tRNA}$) relative to those formed in the E/E state, calculated from simulations that used the baseline model (left). When uL1m-P-tRNA contacts are attenuated (ΔuL1m model; right), $Q_{L1\text{-}tRNA}$ remains low, consistent with a lack of uL1m binding. **c,** In simulations of P/E formation, perturbations to uL1m and/or mL64 (models ΔuL1m, ΔmL64, and ΔmL64-ΔuL1m models) lead to a wider range of tRNA elbow positions and longer timescales for P/E formation. The narrower range of pathways accessed with the complete/baseline model leads to a lower average value of R_{elbow} as a function of the tRNA CCA position R_{CCA},showing how the corridor favors a process where the elbow motion precedes CCA movement. **d,** Probability distribution (327 simulated events) as a function of elbow and 3′-CCA position reveals distinct intermediates during P/E formation. Representative structural snapshots of I1-I3 are shown in panels e-g. **e**, Intermediate I1 is associated with a small displacement of the tRNA elbow and CCA tail toward the E site. **f,** In order to reach I2, the tRNA elbow is displaced by an additional ~10Å, where it it confined by contacts with mL64. **g,** mL64 then guides the tRNA elbow towards the E site, allowing it to adopt I3. After reaching I3, a final ~40Å displacement of the CCA tail results in adoption of the P/E conformation.

Mitoribosome function is independent of mS29 GTPase activity, but GDP stabilizes intersubunit communication

For each translation step, the movement of mRNA:tRNA is also accompanied by the SSU head swiveling, but it has remained an open question whether intrinsic GTPase activity of mS29 (also known as death-associated protein 3, DAP3) is coupled to the process [63, 64]. We now resolve it by analyzing the structure in two different conformations combined with structure-based mutagenesis and biochemical analysis (Fig. 10, Supplementary Fig. 11a-c). Particularly, we performed site-directed mutagenesis targeting the previously reported nucleotide-binding site [2, 63]

425 and found that the mutant K134A, which based on the structure would affect the nucleotide
426 binding, appears to be dispensable for mitoribosomal function (Supplementary Fig. 11a,b).
427 Recently, another putative binding site has been proposed, formed with residues 173, 177, 208,
428 209, 210, 238, 242, 245, 291, 292, 295 [45, 46] (Fig. 10a,b, Supplementary Fig. 11d), and our map at
429 the local resolution of 2.65 Å suggests the presence of GDP in that site. To address the functional
430 relevance of the GDP, we compared it with the SSU structure in the presence of a
431 nonhydrolyzable analog GMPPNP [45] (Fig. 10a,b). It showed a very similar global architecture of
432 mS29, implying that no net conformational change is involved upon GTP hydrolysis (Fig.
433 10a,b). Furthermore, there is no loss of interactions of mS29 with its binding partners in the SSU
434 head (Fig. 10b). Together, the data suggest that the GTPase activity is not coupled to the
435 translation cycle and the related SSU head swiveling.
436 We next used structural and biochemical analysis to identify the role of the GDP. We compared
437 the interactions of mS29, which is the signature protein of the SSU head with the CP between
438 our classical (2.6 Å resolution) and hybrid (3.0 Å resolution) structures. In the classical state,
439 they are extensive and manifest through three contact sites. Site-1 and -2 are formed between
440 GDP-associated region and the respective mL46 helices α2 and α3 extending from the CP.
441 Contact site-3 is formed with mL48 β-turn protruding into the intersubunit space. Upon subunit
442 ratcheting, in the hybrid state mS29 shifts resulting in disruption of contact site-3. Further, the
443 mS29 β-hairpin 208-216 (stabilized by GDP) that formed contact site-2 in the classical state
444 switches in the hybrid state and remains the only inter-subunit bridge in the dimeter of 50 Å (Fig.
445 10c, Supplementary Fig. 11e). To assess the role of GDP binding in translation, we generated
446 cell lines stably expressing mS29 mutants to disrupt the GDP binding site (Fig. 10d-g,
447 Supplementary Fig. 11a-c).
448 Expression of the double mutants R177A/K245A or R177A/K295A, which target residues
449 interacting with the phosphate groups of GDP, led to reduced levels of mitochondrion-encoded
450 proteins and cellular respiration (Fig. 10d-g, Supplementary Fig. 11c), suggesting a stabilizing
451 role for GDP in this pocket. The R177A/K245A mutation shows only a tendency toward a more
452 stringent effect on mitochondrial protein synthesis than the R177A/K295A mutation in our short
453 15 min pulses. However, the effect is significant when looking at the steady-state levels of
454 mtDNA-encoded proteins. (Fig. 10d,e). Interestingly, the double mutant R177A/H291A
455 displayed a rate of mitochondrial protein synthesis comparable to WT (Fig. 10d-g). Although
456 K245 and K295 stabilize the same beta phosphate on GDP, it is possible that H291 can
457 compensate for the loss of K295, explaining the decreased stability of the R177A/K245A mutant
458 compared to the R177A/K295A mutant. Change of nearby hydrophobic residues Y173A/Y208A
459 yields a decrease in translation similar to the R177A/K245A implying their role in GDP
460 stabilization (Fig. 10d-g). Lastly, double mutant pairs V209P/D238A and Y208A/D238A, which
461 directly disrupt GDP base binding to the mS29 β-hairpin, showed drastic decreases in the
462 synthesis and stability of mitochondrion-encoded proteins (Fig. 10d-g). Thus, the biochemical
463 assays based on mutagenesis show that GDP binding to mS29 is required for efficient
464 mitochondrial translation. Our structure-function correlation analyses suggest that GDP acts as a

stabilizing agent for mS29 β-hairpin 208-216 to maintain the intersubunit communication as tRNA moves to the hybrid state.

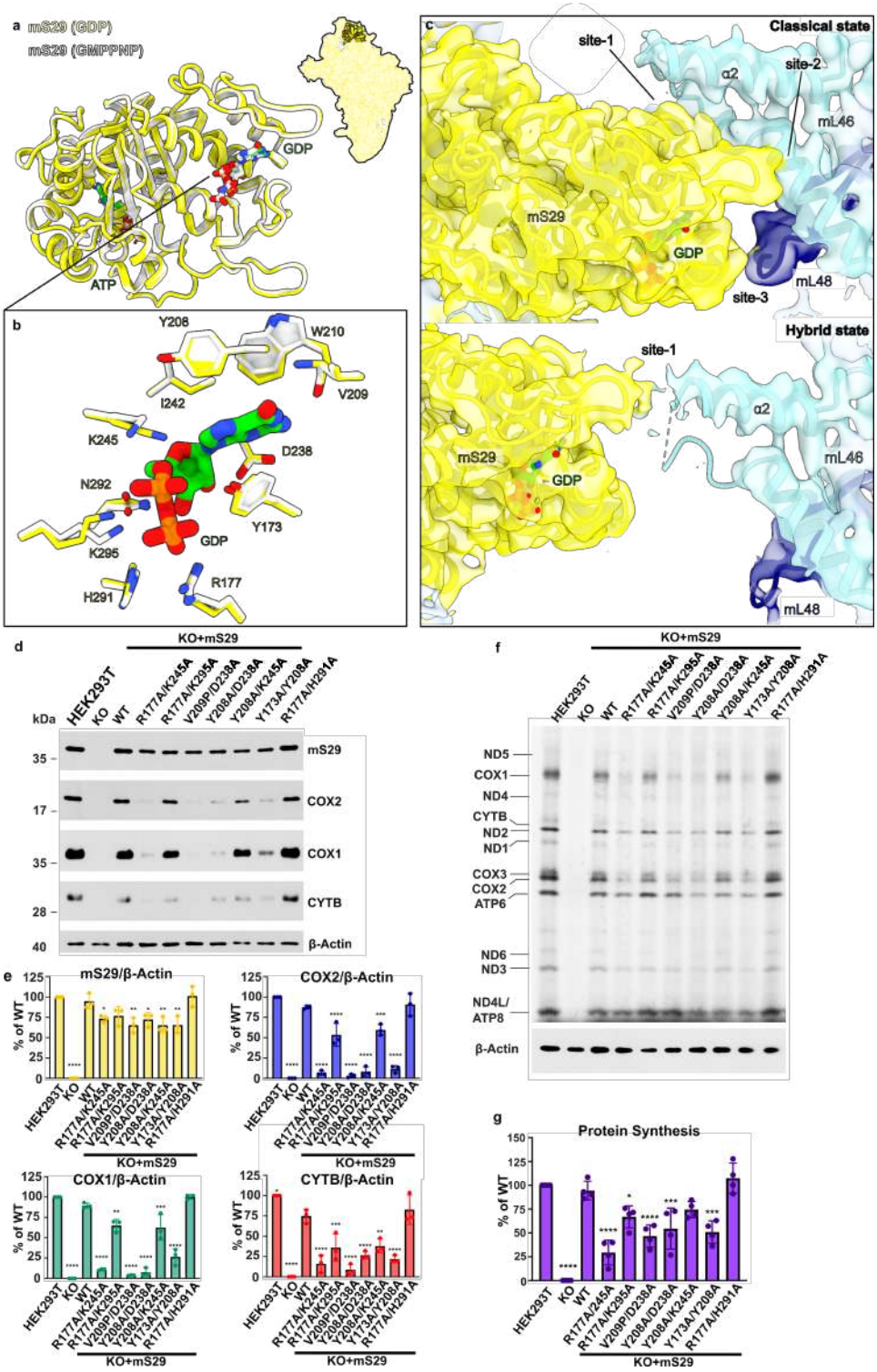

Fig. 10: Binding of GDP to mS29 and role in mitoribosome function.

469 **a,** Superposition of GDP-bound (yellow) and GMPPNP-bound (white) states. **b,** Close-up view
470 illustrating side chains that coordinate nucleotide binding. **c,** Intersubunit contacts in the classical
471 and hybrid states mediated by mS29 (cryo-EM density map shown as colored surface). **d**,
472 Immunoblot analysis comparing steady-state levels of proteins using whole cell lysates from
473 HEK293T (WT), *mS29*-KO (KO), and *mS29*-KO cells stably expressing either WT mS29 or
474 double mutants targeting the GDP-mS29β-hairpin binding site under the control of an attenuated
475 CMV6 promoter (Δ5pCMV6). COX1, COX2, and CTYB were used as markers of mitoribosome
476 function, and β-Actin was used as a loading control. **e**, Images in panel (d) were digitalized, and
477 densitometry was conducted using the histogram function in Adobe Photoshop. The bar graphs
478 represent the mean ± SD from three independent repetitions. Statistical differences were
479 estimated using one-way ANOVA in GraphPad Prism. *p<0.05, **p<0.01; ***p<0.001,
480 ****p<0.0001. **f**, Metabolic labeling of mitochondrially translated peptides in whole cells from
481 the indicated cell lines using ^{35}S-methionine for 15 minutes in the presence of emetine to inhibit
482 cytosolic protein synthesis. Immunoblotting for β-ACTIN was used as a loading control. Newly
483 synthesized peptides are identified on the left. **g**, Images in panel (d) were digitalized, and
484 densitometry was conducted using the histogram function in Adobe Photoshop. The bar graphs
485 represent the mean ± SD from four independent repetitions. Statistical differences were
486 estimated using one-way ANOVA in GraphPad Prism. *p<0.05, **p<0.01; ***p<0.001,
487 ****p<0.0001. The source data file contains all original uncropped and unprocessed
488 immunoblots as well as densitometry values used to perform statistics and generate
489 quantification graphs in panels (d-g).
490

491 **Discussion**

492 This study illustrates the modifications and cofactors of the human mitoribosome (Fig. 1-4,
493 Supplementary Fig. 3-5) and explains how mRNA and tRNAs are stabilized (Fig. 5-9,
494 Supplementary movie 1). While the basic mechanism of translation and the rRNA in the
495 decoding center are conserved, our structures attribute additional roles to mitoribosomal proteins
496 in mRNA and tRNA binding.

497 For mRNA, previous work showed that the delivery of some mitochondrial transcripts for
498 translation is facilitated by the factor LRPPRC [65, 66]. We now demonstrate that once an mRNA is
499 received by the mitoribosome, it involves six mitochondria-specific proteins that sequentially
500 help to direct the mRNA to the decoding center, where it's aligned with a tRNA (Fig. 5,6,
501 Supplementary Fig. 6,8-9). Most of these proteins compensate for the reduced rRNA through the
502 mechanisms of structural patching [67] and protein ratcheting [68] that drive neutral evolution of
503 protein complexity. The first protein to receive an mRNA is mS39, and we detected a co-
504 evolution of mS39 with an mRNA motif Y-N-C-Y that is enriched in all 12 transcripts encoded
505 in the heavy strand of the mitochondrial DNA. The only mRNA that is not enriched with the
506 motif is ND6 (Fig. 5, Supplementary Fig. 7). Interestingly, *ND6* possesses a long 3′UTR and is
507 the only transcript in human mitochondria lacking a polyA tail. This gene is also the only one in
508 mitochondria of vertebrates that was found to be translocated to the control region through gene

509 duplication [69]. This occurs in Antarctic fish species, and while the selectively advantageous
510 duplicate is functionally neutral on the protein level [70], we found that there is a change in the Y-
511 N-C-Y frequency in the mRNA sequence, which is increased by 2-fold (from 14 to 30
512 occurrences in 525 residues). It suggests a possible adaptive correlation between the mRNA
513 stability on the mitoribosome and mt-DNA reorganization.

514 For tRNA, the structure demonstrates two cases with an involvement of mitoribosomal proteins.
515 First, between the A- and P-site tRNAs, the N-terminus of mL40 extends from the CP to the
516 phosphate backbone of mRNA. Second, the recognition of a tRNA in the E-site is achieved by a
517 protein-made L1 stalk region and mL64. Both architectures are unique to mitochondria. Our
518 molecular dynamics simulations further illustrate how the process of E-tRNA movement
519 fundamentally relies on specific protein extensions and insertions of uL1m and uL9m without
520 any involvement of rRNA (Fig. 8,9, Supplementary movie 2). These adaptations of
521 mitoribosomal proteins are particularly important in the context of different functional states, as
522 previous structural studies of elongation [8], termination [10], and rescue [6] complexes reported
523 unidentified densities associated with translational factors, which we now assign specific
524 proteins. Since our data resolves those densities as mammalian protein extensions (Fig. 5,
525 Supplementary Fig. 6), the structural information can now be used for reinterpretation of the
526 functional complexes, thus completing previous works.

527 In addition to proteins, newly revealed structural details include polyamines as stabilizing
528 intramolecular agents in human mitochondria. The visualization of polyamines in the human
529 mitoribosome and the reduced occupancy in the presence of antibiotics further supports their
530 stimulating effect on mitochondrial translation, which is essential for cell proliferation. In
531 mitoribosomes from cell culture treated with antibiotics [45, 71], the occupancy of the polyamines is
532 reduced [45], and they are generally replaced with Mg^{2+}or K^{+}, accompanied by some residue
533 rearrangement (Supplementary Fig. 5). Those changes are associated with attenuation of
534 translation, and thus our structure rationalizes previous report that the positive effect of
535 polyamines could not be functionally replaced by the addition of Mg^{2+} in a cell-free system [72].
536 Together, it links mitochondrial translation to reports assigning key regulatory effects to
537 polyamines in mitochondria. This includes anti-inflammatory effects and inhibition of aging-
538 associated pathologies upon consumption of polyamine in mice [31, 32, 73], the ability to boost
539 mitochondrial respiratory capacity in a *Drosophila* aging model [32], restorative effects on
540 oxidative functions of aged mitochondria [74, 75], and antitumor immunity in aged mice [76].
541 Polyamines were also proposed to regulate mitochondrial metabolism via Src kinase signaling to
542 preserve bioenergetics in the spinal cord [77]. Considering our results on the involvement of iron-
543 sulphur clusters as protein-protein mediating agents [45], as well as in the mitoribosomal assembly
544 [78], the new structural data provides a wealth of additional information on cofactors that can be
545 further assessed in disease models and with respect to tissue and cell specificity, as well as
546 ageing processes. The detection of disulfide bond in mS37 that was proposed to occur during the
547 mitochondrial protein import pathway [47] further links translation with metabolic state and

548 NADH/NAD$^+$ ratio in the intermembrane space and the matrix due to the special role of mS37
549 that links assembly to the initiation of translation [25].
550 On the rRNA level, through tailored quantitative mass-spectrometry, we describe a fully
551 modified mitoribosome, including in the decoding center. While the critical modifications are
552 conserved with bacteria, an unexpected feature of the structure is that the rRNA component CP-
553 tRNA^{Val} is modified, as well as aminoacylated. This suggests that this tRNA is recognized in the
554 matrix by the elongation factor mtEF-Tu prior the assembly onto the CP. The involvement
555 mtEF-Tu in the mitoribosome assembly has been previously reported, and direct interaction with
556 the assembly factor GTPBP5 was visualized by cryo-EM of an LSU intermediate [79]. Thus, the
557 regulation of the assembly of the mammalian mitoribosome relies on the availability of mtEF-Tu
558 in active developmental stages of the organelle, which might be a potential early checkpoint for
559 translation. A possible model for these observations is that accumulation of deacylated tRNAs
560 might trigger starvation responses, and since tRNA^{Val} is likely to be abundant at the onset of
561 mitoribosomal assembly, its aminoacylation is essential, which requires the presence of mtEF-
562 Tu. The feature is likely to be mammalian-specific, as representative from other lineages, such as
563 fungi [46], ciliates [80], and algae [81, 82] do not possess the CP-tRNA component in their
564 mitoribosomes.

565 Finally, the data addresses a long-standing question of whether a putative GTPase and death-
566 associated protein mS29 might provide the human mitoribosome with an intrinsic activity, while
567 undergoing structural rearrangements. This protein is of a particular clinical interest, because
568 several cancer types are associated with its aberrant expression [83]. We show that mS29-GDP
569 does not change its conformation during translation but is a stable structural element that
570 contributes to inter-subunit communication during transitions between classical and hybrid states
571 (Fig. 10, Supplementary Fig. 11).

572 Overall, these data explain how the newly identified components modulate the functional and
573 structurally distinct mitoribosome. With the continuous progress in improvement of resolution of
574 cryo-EM reconstructions, and availability of newly developed methods for base editing of
575 protein-coding genes in mammalian mitochondrial genome [84, 85], the field of mitochondrial
576 translation now steps into a phase, where it becomes possible to analyze fine regulatory
577 mechanisms specific transcripts, and study how it's affected by modifications, cofactors, and
578 mutants. Therefore, the structural approach has a potential to lead towards a more detailed
579 description of the mitoribosome-associated pathologies, including mitochondrial disease and
580 ageing, and the current study will provide a reference model of the human mitoribosome for
581 future investigation.

582

583 **References**

584 1. Kienzle L*, et al.* A small protein coded within the mitochondrial canonical gene nd4
585 regulates mitochondrial bioenergetics. *BMC Biol* **21**, 111 (2023).
586

2. Amunts A, Brown A, Toots J, Scheres SHW, Ramakrishnan V. Ribosome. The structure of the human mitochondrial ribosome. *Science* **348**, 95-98 (2015).

3. Ferrari A, Del'Olio S, Barrientos A. The Diseased Mitoribosome. *FEBS Lett* **595**, 1025-1061 (2021).

4. Amarasekera SSC*, et al.* Multi-omics identifies large mitoribosomal subunit instability caused by pathogenic MRPL39 variants as a cause of pediatric onset mitochondrial disease. *Hum Mol Genet*, (2023).

5. Aibara S, Singh V, Modelska A, Amunts A. Structural basis of mitochondrial translation. *Elife* **9**, (2020).

6. Desai N, Yang H, Chandrasekaran V, Kazi R, Minczuk M, Ramakrishnan V. Elongational stalling activates mitoribosome-associated quality control. *Science* **370**, 1105-1110 (2020).

7. Koripella RK*, et al.* Structures of the human mitochondrial ribosome bound to EF-G1 reveal distinct features of mitochondrial translation elongation. *Nat Commun* **11**, 3830 (2020).

8. Kummer E, Ban N. Structural insights into mammalian mitochondrial translation elongation catalyzed by mtEFG1. *EMBO J* **39**, e104820 (2020).

9. Kummer E*, et al.* Unique features of mammalian mitochondrial translation initiation revealed by cryo-EM. *Nature* **560**, 263-267 (2018).

10. Kummer E, Schubert KN, Schoenhut T, Scaiola A, Ban N. Structural basis of translation termination, rescue, and recycling in mammalian mitochondria. *Mol Cell* **81**, 2566-2582 e2566 (2021).

11. Rebelo-Guiomar P, Powell CA, Van Haute L, Minczuk M. The mammalian mitochondrial epitranscriptome. *Biochim Biophys Acta Gene Regul Mech* **1862**, 429-446 (2019).

12. D'Souza AR, Minczuk M. Mitochondrial transcription and translation: overview. *Essays Biochem* **62**, 309-320 (2018).

13. Garone C*, et al.* Defective mitochondrial rRNA methyltransferase MRM2 causes MELAS-like clinical syndrome. *Hum Mol Genet* **26**, 4257-4266 (2017).

14. Lopez Sanchez MIG, Cipullo M, Gopalakrishna S, Khawaja A, Rorbach J. Methylation of Ribosomal RNA: A Mitochondrial Perspective. *Front Genet* **11**, 761 (2020).

631 15. Antonicka H, Choquet K, Lin ZY, Gingras AC, Kleinman CL, Shoubridge EA. A
632 pseudouridine synthase module is essential for mitochondrial protein synthesis and cell
633 viability. *EMBO Rep* **18**, 28-38 (2017).
634
635 16. Baer RJ, Dubin DT. Methylated regions of hamster mitochondrial ribosomal RNA:
636 structural and functional correlates. *Nucleic Acids Res* **9**, 323-337 (1981).
637
638 17. McCulloch V, Seidel-Rogol BL, Shadel GS. A human mitochondrial transcription factor
639 is related to RNA adenine methyltransferases and binds S-adenosylmethionine. *Mol Cell*
640 *Biol* **22**, 1116-1125 (2002).
641
642 18. Metodiev MD*, et al.* Methylation of 12S rRNA is necessary for in vivo stability of the
643 small subunit of the mammalian mitochondrial ribosome. *Cell Metab* **9**, 386-397 (2009).
644
645 19. Metodiev MD*, et al.* NSUN4 is a dual function mitochondrial protein required for both
646 methylation of 12S rRNA and coordination of mitoribosomal assembly. *PLoS Genet* **10**,
647 e1004110 (2014).
648
649 20. Seidel-Rogol BL, McCulloch V, Shadel GS. Human mitochondrial transcription factor
650 B1 methylates ribosomal RNA at a conserved stem-loop. *Nat Genet* **33**, 23-24 (2003).
651
652 21. Sergiev PV, Aleksashin NA, Chugunova AA, Polikanov YS, Dontsova OA. Structural
653 and evolutionary insights into ribosomal RNA methylation. *Nat Chem Biol* **14**, 226-235
654 (2018).
655
656 22. Van Haute L*, et al.* METTL15 introduces N4-methylcytidine into human mitochondrial
657 12S rRNA and is required for mitoribosome biogenesis. *Nucleic Acids Res* **47**, 10267-
658 10281 (2019).
659
660 23. Zaganelli S*, et al.* The Pseudouridine Synthase RPUSD4 Is an Essential Component of
661 Mitochondrial RNA Granules. *J Biol Chem* **292**, 4519-4532 (2017).
662
663 24. Hillen HS*, et al.* Structural basis of GTPase-mediated mitochondrial ribosome biogenesis
664 and recycling. *Nat Commun* **12**, 3672 (2021).
665
666 25. Itoh Y*, et al.* Mechanism of mitoribosomal small subunit biogenesis and preinitiation.
667 *Nature* **606**, 603-608 (2022).
668
669 26. Harper NJ, Burnside C, Klinge S. Principles of mitoribosomal small subunit assembly in
670 eukaryotes. *Nature* **614**, 175-181 (2023).
671
672 27. Bobba-Alves N*, et al.*, (2022).
673
674 28. Haas RH. Mitochondrial Dysfunction in Aging and Diseases of Aging. *Biology (Basel)* **8**,
675 (2019).
676

29. Hong HJ, *et al.* Mitoribosome insufficiency in beta cells is associated with type 2 diabetes-like islet failure. *Exp Mol Med* **54**, 932-945 (2022).

30. Richman TR, *et al.* Mitochondrial mistranslation modulated by metabolic stress causes cardiovascular disease and reduced lifespan. *Aging Cell* **20**, e13408 (2021).

31. Soda K, Dobashi Y, Kano Y, Tsujinaka S, Konishi F. Polyamine-rich food decreases age-associated pathology and mortality in aged mice. *Exp Gerontol* **44**, 727-732 (2009).

32. Soda K, Kano Y, Chiba F, Koizumi K, Miyaki Y. Increased polyamine intake inhibits age-associated alteration in global DNA methylation and 1,2-dimethylhydrazine-induced tumorigenesis. *PLoS One* **8**, e64357 (2013).

33. Medina CB, *et al.* Metabolites released from apoptotic cells act as tissue messengers. *Nature* **580**, 130-135 (2020).

34. Igarashi K, Kashiwagi K. The functional role of polyamines in eukaryotic cells. *Int J Biochem Cell Biol* **107**, 104-115 (2019).

35. Mandal S, Mandal A, Johansson HE, Orjalo AV, Park MH. Depletion of cellular polyamines, spermidine and spermine, causes a total arrest in translation and growth in mammalian cells. *Proc Natl Acad Sci U S A* **110**, 2169-2174 (2013).

36. Zivanov J, *et al.* New tools for automated high-resolution cryo-EM structure determination in RELION-3. *Elife* **7**, (2018).

37. Zivanov J, Nakane T, Scheres SHW. A Bayesian approach to beam-induced motion correction in cryo-EM single-particle analysis. *IUCrJ* **6**, 5-17 (2019).

38. Zivanov J, Nakane T, Scheres SHW. Estimation of high-order aberrations and anisotropic magnification from cryo-EM data sets in RELION-3.1. *IUCrJ* **7**, 253-267 (2020).

39. Scheres SH. Processing of Structurally Heterogeneous Cryo-EM Data in RELION. *Methods Enzymol* **579**, 125-157 (2016).

40. Taoka M, *et al.* A mass spectrometry-based method for comprehensive quantitative determination of post-transcriptional RNA modifications: the complete chemical structure of Schizosaccharomyces pombe ribosomal RNAs. *Nucleic Acids Res* **43**, e115 (2015).

41. Brown A, *et al.* Structure of the large ribosomal subunit from human mitochondria. *Science* **346**, 718-722 (2014).

42. Brown A, *et al.* Structures of the human mitochondrial ribosome in native states of assembly. *Nat Struct Mol Biol* **24**, 866-869 (2017).

723 43. Greber BJ, *et al.* The complete structure of the large subunit of the mammalian
724 mitochondrial ribosome. *Nature* **515**, 283-286 (2014).
725
726 44. Suzuki T, *et al.* Complete chemical structures of human mitochondrial tRNAs. *Nat*
727 *Commun* **11**, 4269 (2020).
728
729 45. Itoh Y, *et al.* Structure of the mitoribosomal small subunit with streptomycin reveals Fe-S
730 clusters and physiological molecules. *Elife* **11**, (2022).
731
732 46. Itoh Y, Naschberger A, Mortezaei N, Herrmann JM, Amunts A. Analysis of translating
733 mitoribosome reveals functional characteristics of translation in mitochondria of fungi.
734 *Nat Commun* **11**, 5187 (2020).
735
736 47. Peker E, *et al.* A two-step mitochondrial import pathway couples the disulfide relay with
737 matrix complex I biogenesis. *J Cell Biol* **222**, (2023).
738
739 48. Watson ZL, *et al.* Structure of the bacterial ribosome at 2 A resolution. *Elife* **9**, (2020).
740
741 49. Jourdain AA, *et al.* A mitochondria-specific isoform of FASTK is present in
742 mitochondrial RNA granules and regulates gene expression and function. *Cell Rep* **10**,
743 1110-1121 (2015).
744
745 50. Takyar S, Hickerson RP, Noller HF. mRNA helicase activity of the ribosome. *Cell* **120**,
746 49-58 (2005).
747
748 51. Khawaja A, *et al.* Distinct pre-initiation steps in human mitochondrial translation. *Nat*
749 *Commun* **11**, 2932 (2020).
750
751 52. Selmer M, *et al.* Structure of the 70S ribosome complexed with mRNA and tRNA.
752 *Science* **313**, 1935-1942 (2006).
753
754 53. Rozov A, *et al.* Importance of potassium ions for ribosome structure and function
755 revealed by long-wavelength X-ray diffraction. *Nat Commun* **10**, 2519 (2019).
756
757 54. Bhaskar V, *et al.* Dynamics of uS19 C-Terminal Tail during the Translation Elongation
758 Cycle in Human Ribosomes. *Cell Rep* **31**, 107473 (2020).
759
760 55. Ogle JM, Brodersen DE, Clemons WM, Jr., Tarry MJ, Carter AP, Ramakrishnan V.
761 Recognition of cognate transfer RNA by the 30S ribosomal subunit. *Science* **292**, 897-
762 902 (2001).
763
764 56. Youngman EM, Cochella L, Brunelle JL, He S, Green R. Two distinct conformations of
765 the conserved RNA-rich decoding center of the small ribosomal subunit are recognized
766 by tRNAs and release factors. *Cold Spring Harb Symp Quant Biol* **71**, 545-549 (2006).
767

57. Nakayama H, *et al.* Ariadne: a database search engine for identification and chemical analysis of RNA using tandem mass spectrometry data. *Nucleic Acids Res* **37**, e47 (2009).

58. Yamauchi Y, *et al.* A mass spectrometry-based method for direct determination of pseudouridine in RNA. *Nucleic Acids Res* **44**, e59 (2016).

59. Nishimura K, *et al.* Identification of the RsmG methyltransferase target as 16S rRNA nucleotide G527 and characterization of Bacillus subtilis rsmG mutants. *J Bacteriol* **189**, 6068-6073 (2007).

60. Noel JK, *et al.* SMOG 2: A Versatile Software Package for Generating Structure-Based Models. *PLoS Comput Biol* **12**, e1004794 (2016).

61. Whitford PC, Noel JK, Gosavi S, Schug A, Sanbonmatsu KY, Onuchic JN. An all-atom structure-based potential for proteins: bridging minimal models with all-atom empirical forcefields. *Proteins* **75**, 430-441 (2009).

62. Polikanov YS, Melnikov SV, Soll D, Steitz TA. Structural insights into the role of rRNA modifications in protein synthesis and ribosome assembly. *Nat Struct Mol Biol* **22**, 342-344 (2015).

63. Greber BJ, *et al.* Ribosome. The complete structure of the 55S mammalian mitochondrial ribosome. *Science* **348**, 303-308 (2015).

64. Ott M, Amunts A, Brown A. Organization and Regulation of Mitochondrial Protein Synthesis. *Annu Rev Biochem* **85**, 77-101 (2016).

65. Singh V, *et al.* Structural basis of LRPPRC-SLIRP-dependent translation by the mitoribosome. *bioRxiv*, 2022.2006.2020.496763 (2022).

66. Webster MW, *et al.* Structural basis of transcription-translation coupling and collision in bacteria. *Science* **369**, 1355-1359 (2020).

67. Petrov AS, Wood EC, Bernier CR, Norris AM, Brown A, Amunts A. Structural Patching Fosters Divergence of Mitochondrial Ribosomes. *Mol Biol Evol* **36**, 207-219 (2019).

68. Hochberg GKA, Liu Y, Marklund EG, Metzger BPH, Laganowsky A, Thornton JW. A hydrophobic ratchet entrenches molecular complexes. *Nature* **588**, 503-508 (2020).

69. Zhuang X, Cheng CH. ND6 gene "lost" and found: evolution of mitochondrial gene rearrangement in Antarctic notothenioids. *Mol Biol Evol* **27**, 1391-1403 (2010).

70. Mark FC, *et al.* Mitochondrial function in Antarctic nototheniids with ND6 translocation. *PLoS One* **7**, e31860 (2012).

71. Itoh Y, *et al.* Mechanism of membrane-tethered mitochondrial protein synthesis. *Science* **371**, 846-849 (2021).

72. Ogasawara T, Ito K, Igarashi K. Effect of polyamines on globin synthesis in a rabbit reticulocyte polyamine-free protein synthetic system. *J Biochem* **105**, 164-167 (1989).

73. Schroeder S, *et al.* Dietary spermidine improves cognitive function. *Cell Rep* **35**, 108985 (2021).

74. Jing YH, *et al.* Spermidine ameliorates the neuronal aging by improving the mitochondrial function in vitro. *Exp Gerontol* **108**, 77-86 (2018).

75. Phillips JE, Chaffee RR. Restorative effects of spermine on oxidative phosphorylation and respiration in heat-aged mitochondria. *Biochem Biophys Res Commun* **108**, 174-181 (1982).

76. Al-Habsi M, *et al.* Spermidine activates mitochondrial trifunctional protein and improves antitumor immunity in mice. *Science* **378**, eabj3510 (2022).

77. Zhang R, Ma XN, Liu K, Zhang L, Yao M. Exogenous spermine preserves mitochondrial bioenergetics via regulating Src kinase signaling in the spinal cord. *Mol Med Rep* **16**, 3619-3626 (2017).

78. Ast T, *et al.* METTL17 is an Fe-S cluster checkpoint for mitochondrial translation. *bioRxiv*, 2022.2011.2024.517765 (2022).

79. Cipullo M, Gese GV, Khawaja A, Hallberg BM, Rorbach J. Structural basis for late maturation steps of the human mitoribosomal large subunit. *Nat Commun* **12**, 3673 (2021).

80. Tobiasson V, Amunts A. Ciliate mitoribosome illuminates evolutionary steps of mitochondrial translation. *Elife* **9**, (2020).

81. Tobiasson V, Gahura O, Aibara S, Baradaran R, Zikova A, Amunts A. Interconnected assembly factors regulate the biogenesis of mitoribosomal large subunit. *EMBO J* **40**, e106292 (2021).

82. Waltz F, Soufari H, Bochler A, Giege P, Hashem Y. Cryo-EM structure of the RNA-rich plant mitochondrial ribosome. *Nat Plants* **6**, 377-383 (2020).

83. Sui L, *et al.* Death associated protein-3 (DAP3) and DAP3 binding cell death enhancer-1 (DELE1) in human colorectal cancer, and their impacts on clinical outcome and chemoresistance. *Int J Oncol* **62**, (2023).

84. Silva-Pinheiro P, *et al.* A library of base editors for the precise ablation of all protein-coding genes in the mouse mitochondrial genome. *Nat Biomed Eng*, (2022).

85. Willis JCW, Silva-Pinheiro P, Widdup L, Minczuk M, Liu DR. Compact zinc finger base editors that edit mitochondrial or nuclear DNA in vitro and in vivo. *Nat Commun* **13**, 7204 (2022).

Methods

Experimental model and culturing

HEK293S-derived cells (T501) were grown in Freestyle 293 Expression Medium containing 5% tetracycline-free fetal bovine serum (FBS) in vented shaking flasks at 37°C, 5% CO_2 and 120 rpm (550 x g). Culture was scaled up sequentially, by inoculating at 1.5 x 10^6 cells/mL and subsequently splitting at a cell density of 3.0 x 10^6 cells/mL. Finally, a final volume of 2 L of cell culture at a cell density of 4.5 x 10^6 cells/mL was used for mitochondria isolation, as previously described [86].

mS29-KO cells were derived from HEK293T (CRL-3216) and cultured in complete DMEM supplemented with 20% FBS at 37 °C and 5% CO_2. HEK293T (CRL-3216) were cultured in high-glucose, sodium pyruvate, L-glutamine Dulbecco's modified Eagle medium (DMEM, Life Technologies) supplemented with 10% FBS, 100 µg/mL uridine, 3 mM sodium formate, and 1x MEM non-essential amino acids complete DMEM medium). Analysis of mycoplasma contamination was routinely performed.

For the labeling of cells with deuterated Uridine required for SILNAS analysis, TK6 cells deficient in uridine monophosphate synthase (*UMPS-/-*) were cultured at 37°C in RPMI-1640 medium containing 10% horse serum, 2 mM L-glutamine, penicillin (50 U/ml), streptomycin (50 µg/ml) and 0.1 mM 5,6-D2-uridine.

Generation of mS29 edited cell lines and plasmid transfections

To generate a stable human *mS29-KO* cell line in HEK293T cells (ATCC: CRL-3216), we used a pool of CRISPR/Cas9-mediated knockout cells generated by the genome editing company, Synthego (Synthego Corporation, Redwood City, CA). HEK293T cells were first tested to be negative for mycoplasma. Three guide RNAs targeting exon 5 of the *mS29* gene (DAP3-202 transcript ID ENST00000368336.10) were selected for high specificity and activity to create premature stop codons through frameshift mutations in the coding region via insertions and/or deletions (Indels). Targeting exon 5 ensured that all *mS29* transcript variants would be affected. Based on additional off-target analysis, the three specific guide RNAs selected (g1, g2, and g3) were: g1 5′-GUGAAGCUUGCCUGAUGGUA-3′ [AGG]-PAM, g2 5′-UAUAGCUGGAUAAGCAAAAC-3′ [TGG]-PAM, and g3 5′-AUGCUUUCUCCCCUCAAAUA-3′ [AGG]-PAM. The pool of knockout cells was then generated by electroporation of ribonucleoproteins (RNPs) containing the Cas9 protein and synthetic chemically modified sgRNA (Synthego) into the cells using Synthego's optimized protocol. The editing efficiency was assessed upon recovery, 48 h post-electroporation. Genomic

898 DNA is extracted from a portion of the cells, PCR-amplified, and sequenced using Sanger
899 sequencing. The resulting chromatograms are processed using Synthego Inference of CRISPR
900 Edits software (ice.synthego.com). The pooled *mS29-KO* was then plated into 96-well plates to
901 screen for single clones in-house. Single clone candidates were screened by immunoblotting to
902 determine the steady-state levels of mS29 and the mtDNA-encoded COX2 protein as a surrogate
903 of mitochondrial protein synthesis capacity. Clones that had undetectable mS29 and attenuated
904 COX2 levels were further analyzed by genotyping. For genotyping, the edited region of mS29
905 was amplified using oligonucleotides mS29 exon 5 seq (-164) Forward: 5′-
906 GGATAGATTTTCAAACTCAGTACCA-3′ and mS29 exon 5 seq (+166) Reverse: 5′-
907 TCCTGACTTCAGGCGATACG-3′, and subsequently cloned into the TOPO-TA vector
908 (Thermo Fisher) for sequencing.

909 To establish a stable cell line reconstituted with mS29, we obtained the WT *mS29* gene as a
910 Myc/DDK-tagged ORF from Origene (Cat# RC223182). Using restriction sites *Asi*SI and *Pme*I,
911 WT mS29-Myc/DDK was cloned into a mammalian vector with hygromycin as the selection
912 marker. The vector used was pCMV6, in which mS29 gene expression was placed under the
913 control of an attenuated version of the human cytomegalovirus (CMV) enhancer/promoter (Δ5)
914 in which a deletion in the promoter sequence eliminates most transcription factor binding sites [87].
915 Furthermore, to ensure functionality of the recombinant mS29, the Myc/DDK tag was removed
916 via the Q5 site-directed mutagenesis kit (New England Biolabs) using the oligonucleotides mS29
917 ΔMyc-DDK Forward: 5′-TAAACGGCCGGCCGCGGT-3′ and mS29 Δmyc-DDK Reverse: 5′-
918 GAGGTAGGCACAGTGCCGCTC-3′. Two µg of the construct containing *mS29* was
919 transfected to the HEK293T *mS29*-KO cell line using 5 µL of EndoFectin™ Max (GeneCopoeia)
920 pre-incubated in Opti-MEM (ThermoFisher). 72 h post-transfection, the medium was
921 supplemented with 200µg/mL hygromycin B for three weeks. We use the same protocol to
922 establish stable cell lines reconstituted with mutant variants of mS29.

923 Mutant variants of the *mS29*-containing construct were generated using the Q5 site-directed
924 mutagenesis kit (New England Biolabs). Mutagenesis primers were designed using the
925 NEBaseChanger tool. Oligonucleotides used for mutagenesis include: mS29 K134A Forward:
926 5′-GGGAACAGGAGCAACCCTAAGTC-3′; mS29 K134A Reverse: 5′-
927 TTCTCTCCATACAGAAGATATC-3′; mS29 Y173A Forward: 5′-
928 GCAGTCCAGCGCCAACAAACAGC-3′; mS29 Y173A Reverse: 5′-
929 AGAAGATCCCGACAATTTTTC-3′; mS29 R177A Forward: 5′-
930 CAACAAACAGGCCTTTGATCAACCTTTAGAG-3′; mS29 R177A Reverse: 5′-
931 TAGCTGGACTGCAGAAGA-3′; mS29 K245A Forward: 5′-
932 AATTGTGCTGGCAGAGCTAAAGAGGC-3′; mS29 K245A Reverse: 5′-
933 CCAACTGCATCTGTGGCG-3′; mS29 H291A Forward: 5′-
934 AGCACTTGTTGCCAACTTGAGGAAAATGATG-3′; mS29 H291A Reverse: 5′-
935 AATTCCTCGGGGGCAATC-3′; mS29 K295A Forward: 5′-
936 CAACTTGAGGGCAATGATGAAAAATGATTG-3′; mS29 K295A Reverse: 5′-
937 TGAACAAGTGCTAATTCC-3′; mS29 Y208A Forward: 5’-

938 TCAAGAGAAGGCTGTCTGGAATAAGAG -3'; mS29 Y208A Reverse: 5'-
939 ACTTTTATCTGGTTCAGG -3'; mS29 V209P Forward: 5'-
940 AGAGAAGTATCCCTGGAATAAGAGAG -3'; mS29 V209P Reverse: 5'-
941 TGAACTTTTATCTGGTTCAG -3'; mS29 D238A Forward: 5'-
942 GAACGCCACAGCTGCAGTTGGAA -3'; mS29 D238A Reverse: 5'-
943 CTCACCCGTGTTATGCCC -3. All mutant sequences were validated by Sanger sequencing
944 using oligonucleotides Δ5pCMV6 Forward: 5′-CCTCTTCGCTATTACGCCAG-3′, mS29
945 cDNA (308) Forward: 5′-AACCAGCCCTAGAACTTCTGC-3′, and mS29 cDNA (829)
946 Forward: 5′-GAAGATAAAAGCCCGATTGC-3′.
947

948 Mitoribosome purification

949 Mitoribosome purification was carried out based on the previously developed protocol for rapid
950 isolation [86]. HEK293S-derived cells were harvested from the 2 L culture when the cell density
951 was 4.2 x 10^6 cells/mL by centrifugation at 1,000 g for 7 min, 4 °C. The pellet was washed and
952 resuspended in 200 mL Phosphate Buffered Saline (PBS). The washed cells were pelleted at
953 1,000 g for 10 min at 4 °C. The resulting pellet was resuspended in 120 mL of MIB buffer (50
954 mM HEPES-KOH, pH 7.5, 10 mM KCl, 1.5 mM $MgCl_2$, 1 mM EDTA, 1 mM EGTA, 1 mM
955 dithiothreitol, cOmplete EDTA-free protease inhibitor cocktail (Roche) and allowed to swell in
956 the buffer for 15 min in the cold room by gentle stirring. About 45 mL of SM4 buffer (840 mM
957 mannitol, 280 mM sucrose, 50 mM HEPES-KOH, pH 7.5, 10 mM KCl, 1.5 mM $MgCl_2$, 1 mM
958 EDTA, 1 mM EGTA, 1 mM DTT, 1X cOmplete EDTA-free protease inhibitor cocktail (Roche)
959 was added to the cells in being stirred in MIB buffer and poured into a nitrogen cavitation device
960 kept on ice. The cells were subjected to a pressure of 500 psi for 20 min before releasing the
961 nitrogen from the chamber and collecting the lysate. The lysate was clarified by centrifugation at
962 800 x g and 4 °C, for 15 min, to separate the cell debris and nuclei. The supernatant was passed
963 through a cheesecloth into a beaker kept on ice. The pellet was resuspended in half the previous
964 volume of MIBSM buffer (3 volumes MIB buffer + 1 volume SM4 buffer) and homogenized
965 with a Teflon/glass Dounce homogenizer. After clarification as described before, the resulting
966 lysate was pooled with the previous batch of the lysate and subjected to centrifugation at 1,000 x
967 g, 4 °C for 15 minutes to ensure complete removal of cell debris. The clarified and filtered
968 supernatant was centrifuged at 10,000 x g and 4 °C for 15 min to pellet crude mitochondria.
969 Crude mitochondria were resuspended in 10 mL MIBSM buffer and treated with 200 units of
970 Rnase-free Dnase (Sigma-Aldrich) for 20 min in the cold room to remove contaminating
971 genomic DNA. Crude mitochondria were again recovered by centrifugation at 10,000 g, 4 °C for
972 15 min and gently resuspended in 2 mL SEM buffer (250 mM sucrose, 20 mM HEPES-KOH,
973 pH 7.5, 1 mM EDTA). Resuspended mitochondria were subjected to a sucrose density step-
974 gradient (1.5 mL of 60% sucrose; 4 mL of 32% sucrose; 1.5 mL of 23% sucrose and 1.5 mL of
975 15% sucrose in 20 mM HEPES-KOH, pH 7.5, 1 mM EDTA) centrifugation in a Beckmann
976 Coulter SW40 rotor at 28,000 rpm (139,000 x g) for 60 min. Mitochondria seen as a brown band

977 at the interface of 32% and 60% sucrose layers were collected and snap-frozen using liquid
978 nitrogen and transferred to −80 °C.

979 Frozen mitochondria were transferred on ice and allowed to thaw slowly. Lysis buffer (25 mM
980 HEPES-KOH, pH 7.5, 50 mM KCl, 10 mM $Mg(OAc)_2$, 2% polyethylene glycol octylphenyl
981 ether, 2 mM DTT, 1 mg/mL EDTA-free protease inhibitors (Sigma-Aldrich) was added to
982 mitochondria and the tube was inverted several times to ensure mixing. A small Teflon/glass
983 Dounce homogenizer was used to homogenize mitochondria for efficient lysis. After incubation
984 on ice for 5-10 min, the lysate was clarified by centrifugation at 30,000 x g for 20 min, 4 °C. The
985 clarified lysate was carefully collected. Centrifugation was repeated to ensure complete
986 clarification. A volume of 1 mL of the mitochondrial lysate was applied on top of 0.4 mL of 1 M
987 sucrose (v/v ratio of 2.5:1) in thick-walled TLS55 tubes. Centrifugation was carried out at
988 231,500 x g for 45 min in a TLA120.2 rotor at 4 °C. The pellets thus obtained were washed and
989 sequentially resuspended in a total volume of 100 µl resuspension buffer (20 mM HEPES-KOH,
990 pH 7.5, 50 mM KCl, 10 mM $Mg(OAc)_2$, 1% Triton X-100, 2 mM DTT). The sample was
991 clarified twice by centrifugation at 18,000 g for 10 min at 4 °C. The sample was applied on to a
992 linear 15-30% sucrose (20 mM HEPES-KOH, pH 7.5, 50 mM KCl, 10 mM $Mg(OAc)_2$, 0.05% n-
993 dodecyl-β-D-maltopyranoside, 2 mM DTT) gradient and centrifuged in a TLS55 rotor at 213,600
994 x g for 120 min at 4 °C. The gradient was fractionated into 50 µL volume aliquots. The
995 absorption for each aliquot at 260 nm was measured and fractions corresponding to the
996 monosome peak were collected. The pooled fractions were subjected to buffer exchange with the
997 resuspension buffer to dilute away sucrose.

998

999 <u>rRNA mass spectrometry</u>

1000 *Purification of mitochondrial rRNAs*

1001 Mitochondrial rRNAs of the HEK293 cells were extracted from the purified ribosome using
1002 Isogen (Nippon Gene) and stored at -80 °C until use. TK6 cell culture (~1.0×10^9 cells) were
1003 homogenized by Dounce homogenizer with 250 mM sucrose, 1 mM EDTA and 10 mM
1004 Tris−HCl (pH 8.0). The lysate was centrifuged twice at 1500 x g for 3 min at 4 °C, and the
1005 resulting supernatant was further centrifuged at 5000 x g for 10 min to obtain mitochondrial
1006 precipitate. From the precipitate, total mitochondrial RNA (~100 µg) was extracted using TRIzol
1007 Reagent (Thermo Fisher Scientific).

1008 Each mitochondrial rRNA was purified by using reversed-phase LC through a PLRP-S 4000Å
1009 column (4.6 × 150 mm, 10 µm, Agilent Technologies). After applying the mixture of rRNAs
1010 from the purified ribosome or total mitochondrial RNA to the column, the rRNAs were eluted
1011 with a 60-minute linear gradient of 11.5–13.5% (v/v) acetonitrile in 100 mM TEAA (pH 7.0) and
1012 0.1 mM diammonium phosphate at a flow rate of 200 µl/min at 60 °C while monitoring the
1013 eluate at A260 [88].

1014

1015 *LC-MS, MS/MS and MS/MS/MS analysis and database search of RNA fragments*

1016 RNA was digested as described below. Nucleolytic RNA fragments were analyzed with a direct
1017 nanoflow LC-MS system as described [89]. The LC eluate was sprayed online at –1.3 kV with the
1018 aid of a spray-assisting device [89] to a Q Exactive Plus mass spectrometer (Thermo Fisher
1019 Scientific) in negative ion mode. Other settings for MS, MS/MS and MS/MS/MS were as
1020 described [58].

1021 Ariadne [57] was used for database searches and assignment of MS/MS RNA spectra. The
1022 composite of human cytosolic and mitochondrial rRNA and tRNA sequences was used as a
1023 database. The following default search parameters for Ariadne were used: maximum number of
1024 missed cleavages, 1; variable modification parameters, two methylations per RNA fragment for
1025 any residue; RNA mass tolerance, ±5 ppm, and MS/MS tolerance, ±20 ppm. For assignment of
1026 Ψ residues using 5,6-D2-uridine labeled RNAs, the mass table and the variable modification
1027 parameters were altered from default values to "5,6D_CU" and "Ψ", respectively, because both
1028 C and U were labeled with the medium and the pseudouridylation reaction results in the
1029 exchange of the position 5 deuterium of 5,6-D2-uridine to the proton of solvent, providing a −1
1030 Da mass shift [52].

1031

1032 *Internal standard RNAs and SILNAS-based quantitation of the stoichiometry of post-*
1033 *transcriptional modification*

1034 To construct the plasmids for i*n vitro* transcription of internal standard RNAs, DNAs encoding
1035 human 12S and 16S rRNAs were amplified by PCR from the mitochondrial DNA from TK6
1036 cells. The PCR primers used are as follows: HindIII-12S-Forward
1037 TATAAAGCTTAATAGGTTTGGTCCTAGCCTTTCTATTAGC, 12S-*Bam*HI-reverse
1038 ATATGGATCCGTTCGTCCAAGTGCACTTTCCAGTACACTT, *Hind*III-16S-forward
1039 TATAAAGCTTGCTAAACCTAGCCCCAAACCCACTCCACCT and 16S-*Xho*I-reverse
1040 ATATCTCGAGAAACCCTGTTCTTGGGTGGGTGTGGGTATA). The amplified DNAs were
1041 inserted into the multiple cloning sites of plasmid pCDNA3.1 (+) (Thermo Fisher Scientific). To
1042 synthesize RNA, 2 µg of template DNA was incubated and transcribed using Megascript T7 kit
1043 (Thermo Fisher Scientific). When RNA was synthesized, guanosine-$^{13}C_{10}$ 5′-triphosphate,
1044 cytidine-$^{13}C_9$ 5′-triphosphate, or uridine-$^{13}C_9$ 5′-triphosphate solution was used instead of the
1045 respective 5′-triphosphate reagent that contained carbons with a natural isotope distribution. The
1046 RNA was precipitated in ethanol, solubilized in nuclease-free water, and purified further by
1047 reversed-phase LC as described above.

1048 SILNAS-based quantitation was performed as described [90]. In brief, RNA (~100 fmol) from
1049 natural sources or cells grown in guanosine with natural isotope distribution was mixed with an
1050 equal amount of synthetic RNA transcribed *in vitro* with ^{13}C-labeled guanosine and digested
1051 with RNAse T1 (2 ng/µl). For the RNA transcribed with $^{13}C_9$-labeled cytidine and uridine, Rnase
1052 A (0.5 ng/µl) was used as the digestion enzyme. Digestion was carried out in 100 mM TEAA
1053 (pH 7.0) at 37°C. The 1:1 RNA mixing was performed based on the measurement of the

1054 absorbance at 260 nm and ensured later by a correction factor obtained experimentally. After
1055 obtaining the LC-MS spectrum of the digested RNA mixture, the stoichiometry of RNA
1056 modification at each site was estimated by Ariadne program designed for SILNAS [90]. The results
1057 were confirmed by manual inspection of the original MS spectrum to examine whether the
1058 estimates are based on 'uncontaminated' MS signals.

1059

1060 *Other procedures for RNA analysis*

1061 The masses of RNA fragments and a-, c-, w-, and y-series ions were calculated with Ariadne
1062 (http://ariadne.riken.jp/). Sequence-specific Rnase H cleavage of rRNAs was performed as
1063 described [91], using O-methylated RNA/DNA hybrid oligonucleotide complementary to the 12S
1064 and 16S rRNAs,
1065 GmUmUmCmGmUmCm(CAAG)UmGmCmAmCmUmUmUmCmCmAmGmUmAmCmAmC
1066 m and (AmAmCmCmCmUmGm(TTCT)UmGmGmGmUmGmGmGmUm, respectively (where
1067 Nm refers to 2'-O-methyl ribonucleotide and deoxyribonucleotides are indicated in parentheses).

1068

1069 <u>SDS-PAGE and immunoblotting analyses</u>

1070 Whole-cell protein extracts were obtained by solubilization in RIPA buffer (25mM Tris-HCl pH
1071 7.6, 150 mM NaCl, 1% NP-40, 1% sodium deoxycholate, and 0.1% SDS) with 1 mM PMSF and
1072 1x mammalian protease inhibitor. Extracts were cleared by 5 minutes of centrifugation at 10,000
1073 g at 4 °C. Protein concentrations were determined with the Folin phenol reagent. 40-60 µg of
1074 whole-cell protein extracts were separated by SDS-PAGE in the Laemmli buffer system.
1075 Proteins were then transferred to nitrocellulose membranes, subsequently blocked with 5% skim
1076 milk, and then incubated with antibodies against the indicated proteins followed by a second
1077 reaction with anti-mouse or anti-rabbit IgG conjugated to horseradish peroxidase. Signals were
1078 detected by chemiluminescence and exposure to X-ray films. For quantification, the signals in
1079 digitalized images were quantified by densitometry using the histogram function of Adobe
1080 Photoshop. Values were normalized to the signal of β-Actin and plotted as the percentage of WT
1081 using the Prism 8 software.

1082

1083 <u>Pulse labeling of mitochondrial translation products</u>

1084 Mitochondrial protein synthesis was determined by pulse-labeling of 60-70% confluent human
1085 wild-type (WT) HEK293T cells, *MRPS29*-KO HEK293T cells, and knockout cells stably
1086 reconstituted with mutant *MRPS29* variants. Cultures were grown in a medium without
1087 methionine and in the presence of 100 µg/mL emetine to inhibit cytoplasmic translation as
1088 described [92, 93]. Cells were labeled for 15 min at 37 °C with 100 µCi of ^{35}S-methionine
1089 (PerkinElmer Life Sciences, Boston, MA). After incubation, the medium containing ^{35}S-
1090 methionine was removed, the cells were washed once with PBS, and then the cells were
1091 incubated for 5 minutes in complete DMEM to allow recovery. After the short incubation, cells

1092 were washed once more with PBS, collected by trypsinization, and whole-cell protein extracts
1093 were obtained by solubilization with RIPA buffer. 40-50 µg of each sample was separated by
1094 SDS-PAGE on a 17.5% polyacrylamide gel, transferred to a nitrocellulose membrane, and
1095 exposed to X-ray film. Membranes were then probed by immunoblotting to assess the steady-
1096 state levels of β-ACTIN as a loading control. Values were normalized to the signal of β-ACTIN
1097 and plotted as the percentage of WT using the Prism 8 software. Potassium cyanide (KCN)-
1098 sensitive endogenous cell respiration was measured polarographically using a Clark electrode in
1099 the indicated cell lines. Cell respiration rates are presented as nmol of O_2 consumed per one
1100 million cells per minute.

1101

1102 Cryo-EM data acquisition

1103 Five cryo-EM datasets of mitoribosomal complexes were collected in total using EPU 1.9
1104 (Extended Data Table 1). First, 3 µL of ~120 nM mitoribosome was applied onto a glow-
1105 discharged (20 mA for 30 sec) holey-carbon grid (Quantifoil R2/2, copper, mesh 300) coated
1106 with continuous carbon (of ~3 nm thickness) and incubated for 30 sec in a controlled
1107 environment of 100% humidity and 4 ºC. The grids were blotted for 3 sec, followed by plunge-
1108 freezing in liquid ethane, using a Vitrobot MKIV (FEI/Thermofischer). For high resolution
1109 mitoribosome analysis, five separate datasets were collected on FEI Titan Krios
1110 (FEI/Thermofischer) transmission electron microscope operated at 300 keV, using C2 aperture of
1111 70 µm and a slit width of 20 eV on a GIF quantum energy filter (Gatan). A K2 Summit detector
1112 (Gatan) was used at a pixel size of 0.83 Å (magnification of 165,000X) with a dose of 29-32
1113 electrons/$Å^2$ fractionated over 20 frames. A defocus range of -0.6 to -2.8 µm was used. More
1114 detailed parameters for each one of the datasets are listed in Supplementary Table 1.

1115

1116 Cryo-EM data processing

1117 The complete workflows of the mitoribosomal complexes A/A-P/P-E/E, A/P-P/E, L1 stalk,
1118 monosome consensus map, SSU and their 8 masked regions are given in Extended Data Figs. 1
1119 and 2. For all the datasets, beam-induced motion correction and per-frame B-factor weighting
1120 were performed for all data sets using RELION-3.0.2 [36, 37]. Motion-corrected micrographs were
1121 used for contrast transfer function (CTF) estimation with gctf [94]. Unusable micrographs were
1122 removed by manual inspection of the micrographs and their respective calculated CTF
1123 parameters. Particles were picked in RELION-3.0.2 [36, 37] , using reference-free followed by
1124 reference-aided particle picking procedures. Reference-free 2D classification was carried out to
1125 sort useful particles from falsely picked objects, which were then subjected to 3D classification.
1126 3D classes corresponding to unaligned particles and LSU were discarded and monosome
1127 particles were pooled and used for 3D auto-refinement yielding a map with an overall resolution
1128 of 2.9-3.4 Å for the five datasets. Resolution was estimated using a Fourier Shell Correlation cut-
1129 off of 0.143 between the two reconstructed half maps. Finally, the selected particles were
1130 subjected to per-particle defocus estimation, beam-tilt correction and per-particle astigmatism

correction followed by Bayesian polishing. Bayesian polished particles were subjected to a second round per-particle defocus correction. A total of 994,919 particles from all datasets were then pooled and separated into 86 optics groups in RELION-3.1 [38], based on acquisition areas and date of data collection. Beam-tilt, magnification anisotropy and higher-order (trefoil and fourth-order) aberrations were corrected in RELION-3.1 [38]. Subsequently, 509,691 particles from datasets 2-4 were pooled together and subjected to 3D auto-refinement giving a final nominal resolution of 2.21 Å. Masked refinement was performed on the small subunit head, body, mS39 and tail to produce maps of 2.36 Å, 2.31 Å, 2.44 Å and 2.45 Å resolution, respectively and likewise for the SLU body, L10-L7/L12 stalk, CP and L1 stalk to yield maps of 2.08 Å, 2.38 Å, 2.36 Å and 2.89 Å resolution, respectively. To improve the quality of the L1-stalk map, 220,906 monosome particles with high occupancy of E/E-tRNA were pooled and subjected to partial signal subtraction using the mask that retains the E/E-tRNA and L1-stalk, followed by 3D auto-refinement to have a nominal resolution of 2.87 Å (Supplementary Fig. 1 and Supplementary Table 1).

For separating the A/A-P/P-E/E and A/P-P/E states, all 994,919 monosome particles were subjected to signal subtraction using the mask that retains the tRNA binding region. The tRNA binding sites displayed weak densities corresponding to a heterogeneous mixture of tRNAs bound with partial occupancy. Signal subtracted particles were 3D classified without alignment using a mask on the A-site. This yielded two main classes, one with density in the A-site (332,187 particles) and the other lacking it (629,597 particles). Particles with density in the A-site were selected and subjected to a second round of 3D-classification using a mask around the P- and E-sites. Two classes were selected, one with P/P- and E/E-tRNA density and other in hybrid state with P/E-tRNA density. All 3D classifications with signal subtracted particles were performed using a T-value of 400. The subtracted signal was reverted for these two classes, corresponding to the A/A-P/P-E/E state (82,522 particles) and A/P-P/E state (20,143 particles). Following 3D auto-refinement, the nominal resolution of the cosmplexes was 2.63 Å and 2.98 Å, respectively. Masked refinement for the classical state was performed using local masks on SSU head, body, tail, and mS39 to produce maps at 2.72 Å, 2.75 Å, 2.91 Å and 2.93 Å resolution, respectively. For the LSU body, L10-L7/L12, CP, and the L1 stalk regions, the resolution was 2.44 Å, 2.84 Å, 2.78 Å and 3.20 Å, respectively. Masked refinement for the hybrid state was performed using the same local masks as for the classical state but transformed to compensate for the structural differences. This produced maps for the SSU head, body, tail, and mS39 to produce maps of 3.03 Å, 3.07 Å, 3.39 Å and 3.47 Å resolution, respectively. For the LSU body, L10-L7/L12 region, CP, and the L1 stalk masks, the resolution was 2.84 Å, 3.29 Å, 3.25 Å and 3.53 Å, respectively. The maps were then subjected to modulation transfer function correction, automatic *B*-factor sharpening and local resolution filtering using RELION-3.1 (Supplementary Fig. 2, Supplementary Table 1).

1170 Model building and refinement

1171 We started by building a model into the 2.21 Å resolution consensus map. The starting model for
1172 the LSU was taken from PDB ID: 6ZSG, and for the SSU from PDB ID: 6RW4. These models
1173 were rigid body fitted using UCSF Chimera [95]. Individual local-masked refined maps with local-
1174 resolution filtering and *B*-factor sharpening (RELION 3.1) superposed to the overall map were
1175 combined into a single composite map using Phenix.combine_focused_maps [96] for model
1176 building and refinement. *Coot* v0.9 [97] with Ramachandran and torsion restraints was used for
1177 model building.

1178 The L1-stalk model was built using the 2.87 Å resolution masked-refined map of L1 stalk from
1179 E/E-tRNA-containing particles. Initial model for uL1m was generated by homology-modeling
1180 with uL1 structure of *T. thermophilus* (PDB ID: 3U4M) as template using the Swiss-Model
1181 webserver [98]. The N-terminal extension of uL1m (residues 61–93), the C-terminal domain
1182 (residues 158–254) and the preceding loop (residues 148–157) of uL9m, and H76-77 (residues
1183 2761–2786) of 16S rRNA were modeled manually into the density. Mitochondria-specific C-
1184 terminal extension of uL9m was modeled as a helix based on the density and secondary structure
1185 prediction by PSIPRED [99]. The model was rigid body fitted into the respective local-masked
1186 refined maps for L1 stalk region in the A/A P/P E/E and A/P/E states followed by self-restrained
1187 real space refinement in *Coot* v0.9.

1188 In the CP, the $tRNA^{Val}$ could be completely modeled, owing to the improved resolution of the
1189 local masked-refined map (2.36 Å). The 3′-CCA terminus (C74–A76) and a valine residue linked
1190 to A76 could be placed on the density map. The N-terminus of mL40 was extended by 13-
1191 residues (47–59) modeled in a tubular wedged between the A- and P-site tRNAs to the phosphate
1192 backbone of mRNA residue 7. Similarly, the C-terminus of bL31m was extended by 31 residues
1193 (95–125) from the C-terminal helix onto SSU head. The local resolution was sufficient for
1194 accurate side-chain modeling for most residues and secondary-structure assignments. We
1195 modeled a disulfide linkage between C45-C76 of mS37. However, they might exist in both
1196 disulfide-linked, and reduced states as indicated by the density and a water mediated hydrogen
1197 bond with a neighbouring Arginine side chain (R240 from uS7m). The other pair C55-C66
1198 appears to be reduced. However, as we had added 1mM DTT to our ribosome purification
1199 buffers, this is not truly indicative of the native state of C45-C76 or C55-C66 pairs.

1200 At the mRNA channel entrance, a more accurate and complete model of mS39 could be built
1201 with 29 residues added to the structure. Improved local resolution enabled unambiguous
1202 assignment of residues to the density which allowed us to address errors in the previous model.
1203 Finally, a total of 28 α-helices could be modeled in their correct register and orientation. Further,
1204 a 28-residue long N-terminal loop of mS31 (residues 247–275) along mS39 and mitochondria-
1205 specific N-terminal extension of uS9m (residues 53–70) approaching mRNA were modeled
1206 manually by fitting the loops into the density maps.

1207 Polyamines were identified upon a further manual inspection of the density map for the presence
1208 of continuous tubular densities which corresponded to spermine, spermidine or putrescine in

length. A total of one spermine, four spermidines and one putrescine were placed in the model, justified by the electrostatic and hydrogen-bonding interactions that each polyamine exhibits at its amine groups with its neighbors.

Metal ions, Mg^{2+}, K^{+} and Zn^{2+}, were modeled into densities based on a manual inspection of small density blobs and the chemical environment, specifically, coordination geometry and strength of density in both unsharpened and local resolution filtered maps. The coordination distance of Mg^{2+} is around 2 Å with an octahedral geometry, whereas that of K^{+} is around 3 Å with more relaxed constraints on coordination geometry. Notably, a density that was modeled previously as Zn^{2+} coordinated by residues D224, D240, D241 and H93 of uS2m was assigned as a magnesium ion, indicated by the octahedral geometry of coordination with the uS2m residues mentioned above and two water molecules.

A-, P- and E-site tRNAs, and mRNA were modeled manually in the density. The density for tRNAs and mRNAs comes from a natively-bound heterogeneous population. Hence, individual residues were modeled as one of the nucleotides, A, U, G, or C, based on the density and/or conservation. While the 70 residues of P-site tRNA could be modeled, fewer residues could be modeled for the A-site (22 residues) and E-site tRNAs (43 residues), including the acceptor arm and anticodon loop due to weaker respective densities. Along the mRNA channel, 34 residues of mRNA were built. In the tRNA binding region, codon-anticodon pairs were clearly resolved. Additionally, extra residues near the A-site (10-12, 14-16) and at the mRNA channel entrance (25, 27-29) were modeled accurately into density. For the remaining mRNA chain at a relatively lower resolution, correct overall chain trace and nucleotide orientation could be assigned. This allowed specific protein-nucleotide interactions to be identified for uS5m, uS7m, uS9m, uS12m, mS35, mS39 and mL40.

For modeling the classical A/A P/P E/E- and hybrid A/P P/E-states, the LSU and SSU from the consensus model were fitted into their composite maps, followed by manual revision. As described above, tRNAs and mRNA were modeled manually into the density.

The water molecules were automatically picked by *Coot* v0.9 [62], followed by manual revision. Geometrical restraints of modified residues and ligands used for the refinement were calculated by Grade Web Server (http://grade.globalphasing.org) or obtained from CCP4 library [100]. Hydrogens were added to the models except for water molecules by REFMAC5 [101] using the prepared geometrical restraint files. Charged α-amino-group hydrogens (H2 and H3) and a free-ribose hydrogen HO3′ were removed from non-terminal protein and RNA residues, respectively, while those at terminal residues were kept. Protonation of Histidine residues were judged based on the chemical environment and removed or kept their N-H hydrogens (HD1 and HE2) accordingly. Protonation/deprotonation of ligands and modified residues were also adjusted.

Final models were further subjected to refinement with Phenix.real_space_refine v1.13_2998 [96], wherein three macro-cycles of global energy minimization with reference restraints (using the input model as the reference, sigma 5-7) and secondary structure restraints, rotamer restraints but without Ramachandran restraints were carried out for each model. The composite maps were

1248 used as the targets for the refinement. An 'edit' file that defines metal-coordination bonds was
1249 generated by ReadySet in the Phenix suite and used. Non-canonical covalent bonds, which are
1250 those between $tRNA^{Val}$ and Valine and between 1-methyl-isoaspartate 184 and G185 in uS11m,
1251 were also defined in the 'edit' file. Model refinement data are listed in Supplementary Table 1.

1252

1253 Bioinformatic analysis of the Y-N-C-Y motif

1254 The density and base-specific interactions of mRNA residues 25-28 with mS39 imply a sequence
1255 of pyrimidine, any nucleotide, cytosine, pyrimidine, leading to a consensus motif: Y-N-C-Y. We
1256 explored the possibility of increased frequency of this motif in mRNA sequences. The sequences
1257 for all 13 mRNAs were obtained from GenBank. The consensus motif was searched in each
1258 sequence and all occurrences (including ones that overlap) were recorded and used to calculate
1259 the percentage frequency of occurrence for each transcript and the average percentage frequency.
1260 To determine if there is an enrichment of this motif in mRNAs, we calculated its occurrence in a
1261 set of nuclear-encoded mRNAs. To create this set, we acquired sequences randomly from
1262 GenBank and subjected them to a 90% redundancy cut-off, resulting in a total of 1369
1263 sequences. The percentage frequency of occurrence of Y-N-C-Y motif was determined for each
1264 of the 1370 sequences and used to calculate an average percentage frequency for the entire set.
1265 Next to determine the distribution of the Y-N-C-Y motif across the length of mRNAs, each
1266 occurrence was plotted against its position number in the mRNA sequence. This distribution for
1267 all 13 mRNA sequences was plotted together for comparison.

1268

1269 Molecular Dynamics simulations: Modified force fields for simulating a truncated mL64 protein
1270 and modified interactions with protein uL1m

1271 *Baseline force field used for simulations of P/E formation*

1272 An all-atom multi-basin structure-based "SMOG" model [60, 61] of the mitoribosome was used to
1273 simulate P/E formation. For this, we first constructed single-basin structure-based models for the
1274 pre- and post-translocation configurations (A/A-P/P and P/P-E/E). We then combined the two
1275 models, such that the composite model stabilizes both the pre- and post-translocation
1276 configurations. Here we describe the baseline model, which is described in the main text. In
1277 subsequent sections, we provide detailed descriptions of all modified force fields.

In a single-basin all-atom structure-based model, every non-hydrogen atom is represented by a bead of unit mass, and an experimentally-obtained structure is used to define the potential energy minimum. The functional form of the potential is given by:

$$U = \sum_{\text{bonds}} \frac{\epsilon_r}{2}(r_i - r_{i,0})^2 + \sum_{\text{angles}} \frac{\epsilon_\theta}{2}(\theta_i - \theta_{i,0})^2$$

$$+ \sum_{\text{impropers}} \frac{\epsilon_{\chi_{imp}}}{2}(\chi_i - \chi_{i,0})^2 + \sum_{\text{planars}} \epsilon_{\chi_{planar}}[1 - \cos(2\chi_i)]$$

$$+ \sum_{\substack{\text{backbone}\\\text{dihedrals}}} \epsilon_{bb} F(\phi_i - \phi_{i,0}) + \sum_{\substack{\text{sidechain}\\\text{dihedrals}}} \epsilon_{sc} F(\phi_i - \phi_{i,0})$$

$$+ \sum_{\text{contacts}} \epsilon_c \left[\left(\frac{\sigma_{ij}}{r_{ij}}\right)^{12} - 2\left(\frac{\sigma_{ij}}{r_{ij}}\right)^{6} \right] + \sum_{\text{non-contacts}} \epsilon_{nc} \left(\frac{\sigma_{nc}}{r_{ij}}\right)^{12}$$

where

$$F(\phi) = [1 - \cos(\phi)] + \frac{1}{2}[1 - \cos(3\phi)]$$

r_0 and θ_0 parameters are assigned values found in the Amber ff03 force field [102]. The dihedral parameters ϕ_0 are defined by the experimental structure. χ_0 non-planar improper dihedrals (around chiral centers) are also defined to have the values adopted in the experimental structures. Planar dihedral angles are given a cosine term with periodicity 2 and minima at 0 and 180 degrees. The energy scale is set to $\epsilon_r = 100\frac{\epsilon}{A^2}, \epsilon_\theta = 80\frac{\epsilon}{rad^2}, \epsilon_{\chi_{imp}} = 10\frac{\epsilon}{rad^2}, \epsilon_{\chi_{planar}} = 40\frac{\epsilon}{rad^2}$, where ϵ is the reduced energy scale. The dihedral and contact energy scales $\epsilon_{bb}, \epsilon_{sc}, \epsilon_C$ are normalized as in Ref. [60].This combination of structure-based non-bonded terms and AMBER bonded terms is identical to the implementation of a previous SMOG-amber variant (called SBM_AA-amber-bonds [103] in the SMOG 2 force field repository (smog-server.org), though post-transcriptionally-modified residues were added for the current model. Upon publication, the SMOG 2 force field templates used in the current study will be available for download on the SMOG 2 force field repository (ID: AA_PTM_Hassan21.v1).

For the non-bonded interactions, each atomic contact that is found in the experimental structure (i.e. "native'' contact) is given an attractive Lennard-Jones-like interaction that stabilizes a preassigned structure. Native contacts were defined based on the Shadow Contact Map algorithm with default parameters [104]. Σ_{ij} are the interatomic distances between contacts in the native structure, multiplied by 0.96. As employed previously in simulations of the ribosome [105, 106] and viral capsids [103], this scaling of the contact distance was employed to avoid artificial expansion of the ribosome that results from thermal energy. That is, while the potential energy is defined such that the experimental structure is the global minimum, thermal energy leads to a free-energy minimum for which the ribosome is slightly expanded. By shortening the stabilizing interactions, the free-energy minimum is consistent with the experimental structure. For this comparison, the radius of gyration (R_g) was used as a measure of expansion. With this scaling of the contact

distances, R_g was found to match that of the cryo-EM model. All non-native contacts are given a repulsive term that ensures excluded-volume steric interactions are present. The parameter σ_{nc} is given the value 2.5 Å, while $\epsilon_{nc} = 0.1\epsilon$.

Stabilizing intra-ribosome contacts and dihedrals were assigned the values found in the A/P-P/E (SSU rotated) hybrid structure, which is described in the main text. This ensures that the SSU rotates forward in each simulation. Each simulation is initiated from the A/A-P/P conformation. All intra-mt-tRNA and intra-mt-mRNA contacts were defined based on the A/A-P/P structure. Since stabilizing contacts in a structure-based model describe effective interactions [107, 108], we rescaled the strengths of subsets of contacts within the model. Consistent with recent simulations of P/E formation in bacteria [105], interactions that stabilize the structure of the ribosome (i.e. intra-ribosomal) are given larger weights than contacts that are only transiently-formed (e.g. tRNA-ribosome contacts). Relative to intra-ribosome contacts, the energetic interactions between the mt-mRNA-tRNA complex and the SSU (in A/A-P/P and P/P-E/E structures) were rescaled by a factor of 0.3. While these interactions were weaker than intra-ribosomal contacts, since the simulations were not performed under conditions in which translocation will occur (*e.g.*, binding of elongation factors or back-rotation, etc), the mt-mRNA maintained its initial position on the mRNA track of the SSU. P/P-E/E contacts between the mt-tRNA and the uL1m protein were rescaled by a factor of 0.8 and all other interactions between mt-mRNA-tRNA and the LSU were rescaled by a factor of 0.1. This rescaling was applied to account for the transient nature of mt-mRNA-tRNA binding to the ribosome. The strength of the uL1m-tRNA contacts was set such that the P/E configuration would stably form contacts with the uL1m protein. When contacts were scaled below a factor of ~0.5, we found that uL1m could not form stable interactions with the mt-tRNA.

Interactions between the 3′-CCA ends of A-site and P-site mt-tRNAs with the A-site and the P-site were scaled by a factor of 0.2, while their interactions with P-site and E-site were scaled by a factor of 0.8. This leads to the mt-tRNA molecules favoring binding of their target sites (*i.e.*, sites bound in the P/E configuration) on the ribosome. While the interactions with the subsequent binding site (*i.e.*, A-site mt-tRNA with the P-site and P-site mt-tRNA with the E-site) were stronger, these contacts are short range (~6 Å). Accordingly, the stronger weights do not affect the dynamics of the mt-tRNA until it is very close to the binding site. Thus, the details of the final repositioning of the 3′-CCA tail of the P-site mt-tRNA should not be overinterpreted. While the contacts are short-range, the structure of the mitoribosome may introduce steric barriers that the mt-tRNA must navigate in order to adopt the P/E configuration [108]. With these considerations in mind, the current model is aimed at identifying structural elements that can impose steric limitations on mt-tRNA during P/E formation.

There were also two sets of harmonic potentials that were introduced. To mimic the presence of a nascent peptide chain, which would restrain the 3′-CCA end of the A-site tRNA to the PTC, we introduced weak harmonic restraints (weight of $1/nm^2$) between the 3′-CCA end of the A-site tRNA and the P site of the LSU. Distances were assigned based on the P/P conformation. These weak interactions ensured that the 3′-CCA end remains localized to the PTC. We also

introduced harmonic potentials between base-pairing contacts in the mt-tRNA acceptor arm (weight 1000/nm^2). Due to the details of the contact map, initial simulations exhibited partial unfolding/refolding of the acceptor arm during P/E formation. Since that was likely an artifact due to the simplicity of the model and the details of the contact map definition, these additional harmonic terms were introduced to ensure the tRNA acceptor arm remained folded throughout the transition.

Modified force fields

Multiple variants of the model (*i.e.*, force field) were considered, in order to investigate the influence of steric interactions between the P-site mt-tRNA and C-terminal residues of mL64 and to investigate the influence of attractive interactions between uL1m and P-site mt-tRNA on P/E formation.

Truncated-mL64 model: ΔmL64 force field

The C-terminal region of mL64 is involved in steric interactions with the mt-tRNA. For ΔmL64 model, the C-terminal region of mL64 (beginning with Q112) was removed from the system. Q112 was chosen as truncating here guarantees no steric interactions between mL64 and the mt-tRNA and keeps the rest of the protein intact. Thus, all other interactions were unperturbed. This model is intended to mimic an ideal experiment, where one could delete the terminal region of mL64 without introducing indirect effects on the dynamics. In our application, this model allows us to ask what effect steric interactions between P-site mt-tRNA elbow and mL64 have on the dynamics of P/E formation. Deletion of this region from the model was achieved using the smog_extract tool of the SMOG 2 software package [60].

Modified-uL1m model: ΔuL1m force field

All stabilizing contacts between uL1m and the P-site mt-tRNA that are formed in the P/P-E/E state were scaled by a relative factor of 0.1, rather than 0.8 (baseline model, above). Thus, by weakening the attractive interactions, there is insufficient stabilizing energy between uL1m and the P/E tRNA, such that the tRNA elbow does not fully reach the P/E configuration.

Combined truncated mL64 and modified uL1m model: ΔmL64-ΔuL1m force field

All modifications applied in the truncated mL64 model and the modified-uL1m model were included in a single combined force field.

Simulation details

All simulations were initiated from the pre-translocation A/A-P/P configuration. All force field files were generated using the SMOG 2 software package [60]. Molecular dynamics simulations

were performed using Gromacs (v5.1.4) [109, 110]. Reduced units were used in all calculations. Energy minimization was first performed using steepest descent minimization. The system was then coupled to a heat bath using Langevin Dynamics protocols, with reference temperature of 0.5 ε/k_B reduced temperature units (60 Gromacs units). This temperature was chosen since it has been shown to produce structural fluctuations that are consistent with those inferred from anisotropic *B*-factors and explicit-solvent simulation [111]. The timestep was 0.002 reduced units and each simulation was continued until the distance of the 3'-CCA end from the LSU E-site R_{CCA} reached a value less than 4 Å. Energy minimization was initially performed using steepest descent minimization. Each simulation was performed for a maximum of 10^8 timesteps. For the primary/baseline model described in the main text (327 simulations) we obtained an aggregate simulated time of 2.27 $*10^6$ reduced units. For the truncated mL64 model (ΔmL64 model) (321 simulations), the aggregate simulation time was 1.87 $*10^6$ reduced units. For the attenuated uL1m contacts model (ΔuL1m model) (237 simulations), the aggregate simulation time was 1.76 $*10^6$ reduced units. For the ΔmL64-ΔuL1m model (181 simulations), the aggregate simulation time was 1.04 * 10^6. Previous comparisons of diffusion coefficients of tRNA molecules in the ribosome (explicit-solvent simulations vs. SMOG models), estimate that 1 reduced unit corresponds to an effective timescale of approximately 1 nanosecond [112]. Using this conversion factor, the presented simulations represent an aggregate effective simulate time of ~ 6.94 milliseconds.

Structural metrics for describing simulated dynamics

- A-site mt-tRNA, R^P_{CCA}: distance between the geometric centers of the side chains of C75 in the A-site mt-tRNA and Gm2815 in the LSU rRNA. These residues base pair in the A/P-P/E and P/P-E/E configurations.

- P-site mt-tRNA, R^P_{CCA}: distance between the geometric centers of the side chains of C75 in the P-site mt-tRNA and Gm2815 in the LSU rRNA. These residues base pair in the A/P-P/E configuration.

-R_{CCA}: distance between the geometric centers of the side chains of A76 in the P-site mt-tRNA and G2909 in the LSU rRNA. G2909 in the E-site forms a base stacking interaction with A76 of P-site mt-tRNA in the A/P-P/E configuration.

-R_{elbow}: distance between geometric centers of U54 of P-site mt-tRNA and its reference position in the A/P-P/E configuration after alignment of the LSU rRNA.

- $Q_{\mathrm{L1-tRNA}}$: the fraction of P/P-E/E contacts between uL1m and P-site mt-tRNA. A contact is defined as formed if it is within a factor of 1.2 of the distance found in the P/P-E/E configuration.

SSU rotation and tilt angles

To follow the rotary motions of the SSU body with respect to the LSU, we calculated rotation and tilt angles for both the SSU body. For this, we first determined the corresponding *E. coli* numbering of the mitoribosome rRNA residues via STAMP alignment [113] of the mitoribosome to

a reference *E. coli* structure (PDB ID: 4V9D). Alignment was performed separately for the LSU, SSU head and SSU body. The angles were then calculated, using the assigned *E. coli* numbering.

Structural model preparation for simulations

Since the cryo-EM models did not resolve the exact same set of atoms, there was a need to perform some additional structural models prior to performing simulations. For example, to define the multi-basin structure-based model, it was necessary for each mt-tRNA molecule to have identical atoms in the pre- and post-translocation configurations. Additionally, to define the intra-ribosome interactions to stabilize the A/P-P/E conformation, it was necessary that all mt-rRNA and mitoribosomal proteins had identical atomic composition. While most of the resolved atoms are common to all reported models, we employed restraint-based modeling to construct models of the mitoribosome and mt-tRNA that have identical compositions. Below, we describe the steps required for modeling the mitoribosome and mt-tRNA.

Structural modeling pre-processing steps for rRNA and proteins for simulations

Since the structure-based model only included intra-ribosome interactions from the A/P-P/E structure, we first removed all mt-tRNA and mt-mRNA from the A/A-P/P and A/P-P/E models. We also removed ligands and water molecules (HOH, SPD, PUT, NAD, SPM). For the remaining atoms, we identified all atoms that were common to the A/A-P/P and A/P-P/E structures. We then generated a single-basin structure-based model of the A/A-P/P structure. Next, position restraints (harmonic terms, weight of 100 for each atom) were introduced for all common atoms, with positions corresponding to the A/P-P/E structure. The system was then energy minimized via steepest descent minimization. Then, the system was subject to simulated annealing. The system was initially simulated at 0.15 reduced temperature units for 25,000 timesteps. The temperature was then linearly decreased to 0 over the next 50,000 timesteps. An additional 25,000 steps were simulated at temperature 0. The final, annealed structural model was used for force field generation steps, as described above.

Structural modeling pre-processing steps for mt-tRNA and mt-mRNA

Since the cryo-EM reconstructions reported consensus/average sequences for each mt-tRNA, the composition of the A-, P- and E-site mt-tRNAs were not identical. To perform simulations, we homogenized the composition of the mt-tRNA molecules in the A/A-P/P-E/E structure and the mt-tRNA codons. For this, we started with the structural model of the A-site mt-tRNA (and the associated codon) from the A/A-P/P structure, and then used it to generate a structure-based model. We then introduced position restraints based on the positions of the A-site mt-tRNA in the A/A-P/P-E/E structure. All common atoms (*i.e.*, backbone atoms, or atoms in identical residues) were restrained to the A-site mt-tRNA/mRNA positions. For the A-site mt-tRNA, restraints were not imposed on residues 46-58 and 16-17. Cycles of minimization and annealing

were performed, where the position restraints were given weights of 1, 10, 100 and then 1000. This process was repeated for the P-site and E-site mt-tRNAs, as well as for the upstream and downstream mt-mRNA. This process produced a model of the A/A-P/P-E/E configuration that has repeating codons and identical mt-tRNA composition. This structural model was used to define the pre-translocation and post-translocation structure-based models, which were used to construct the multi-basin model.

Describing the sequence of rearrangements in simulations

To describe the dynamics of the P-site mt-tRNA during P/E state formation, we have defined three states based on the 2D probability distribution of R^E_{elbow} and R^E_{CCA} distances (Fig. 8). These states are defined as all configurations of the P-site mt-tRNA in the baseline model that sample the following values of R^E_{elbow} & R^E_{CCA}:

state I_1: disk centered at (R^E_{elbow},R^E_{CCA})=(46,35) Å with radius r=6 Å

state I_2: disk centered at (R^E_{elbow},R^E_{CCA})=(63,23) Å with radius r=8 Å

state I_3: disk centered at (R^E_{elbow},R^E_{CCA})=(42,13) Å with radius r=7 Å

Using this definition of the intermediate states, the most common sequence of transitions followed the order P/P => I_1 => I_2 => I_3 => P/E.

Structure analysis and Fig.s

Visualization and analysis of the models and maps was carried out using UCSF Chimera and ChimeraX [95, 114]. For model and map comparisons, models were superposed in *Coot* v0.9 [62] using the Secondary Structure Matching algorithm and maps downloaded from EMDB were resampled on our maps in UCSF Chimera. Simulated snapshots were visualized using Visual Molecular Dynamics [115].

Quantitation and statistical analysis

All experiments were done in at least biological triplicate unless otherwise stated. GraphPad Prism 8 software was used for statistical analyses of the data. One-way analysis of variance (ANOVA) was performed, comparing the mean of each cell line with the mean of the mS29-KO cell line reconstituted with WT mS29, followed by Dunnett's multiple comparisons test. The data is presented as the mean ± SD; * $P \leq 0.05$, ** $P \leq 0.01$, *** $P \leq 0.001$, **** $P \leq 0.0001$. For immunoblotting, band density is quantified and normalized to ACTIN. For metabolic labeling of mitochondrially translated peptides in whole cells, the data presented represents the mean of each sample's ^{35}S signals.

Additional References

86. Aibara S, Andrell J, Singh V, Amunts A. Rapid Isolation of the Mitoribosome from HEK Cells. *J Vis Exp*, (2018).

87. Morita E, Arii J, Christensen D, Votteler J, Sundquist WI. Attenuated protein expression vectors for use in siRNA rescue experiments. *Biotechniques* **0**, 1-5 (2012).

88. Yamauchi Y*, et al.* Denaturing reversed phase liquid chromatographic separation of non-coding ribonucleic acids on macro-porous polystyrene-divinylbenzene resins. *J Chromatogr A* **1312**, 87-92 (2013).

89. Nakayama H, Yamauchi Y, Taoka M, Isobe T. Direct identification of human cellular microRNAs by nanoflow liquid chromatography-high-resolution tandem mass spectrometry and database searching. *Anal Chem* **87**, 2884-2891 (2015).

90. Taoka M*, et al.* Landscape of the complete RNA chemical modifications in the human 80S ribosome. *Nucleic Acids Res* **46**, 9289-9298 (2018).

91. Taoka M*, et al.* The complete chemical structure of Saccharomyces cerevisiae rRNA: partial pseudouridylation of U2345 in 25S rRNA by snoRNA snR9. *Nucleic Acids Res* **44**, 8951-8961 (2016).

92. Bourens M, Barrientos A. A CMC1-knockout reveals translation-independent control of human mitochondrial complex IV biogenesis. *EMBO Rep* **18**, 477-494 (2017).

93. Leary SC, Sasarman F. Oxidative phosphorylation: synthesis of mitochondrially encoded proteins and assembly of individual structural subunits into functional holoenzyme complexes. *Methods Mol Biol* **554**, 143-162 (2009).

94. Zhang K. Gctf: Real-time CTF determination and correction. *J Struct Biol* **193**, 1-12 (2016).

95. Pettersen EF*, et al.* UCSF Chimera--a visualization system for exploratory research and analysis. *J Comput Chem* **25**, 1605-1612 (2004).

96. Afonine PV*, et al.* Real-space refinement in PHENIX for cryo-EM and crystallography. *Acta Crystallogr D Struct Biol* **74**, 531-544 (2018).

97. Emsley P, Cowtan K. Coot: model-building tools for molecular graphics. *Acta Crystallogr D Biol Crystallogr* **60**, 2126-2132 (2004).

98. Waterhouse A*, et al.* SWISS-MODEL: homology modelling of protein structures and complexes. *Nucleic Acids Res* **46**, W296-W303 (2018).

99. Buchan DWA, Jones DT. The PSIPRED Protein Analysis Workbench: 20 years on. *Nucleic Acids Res* **47**, W402-W407 (2019).

100. Krissinel EB, *et al.* The new CCP4 Coordinate Library as a toolkit for the design of coordinate-related applications in protein crystallography. *Acta Crystallogr D Biol Crystallogr* **60**, 2250-2255 (2004).

101. Murshudov GN, *et al.* REFMAC5 for the refinement of macromolecular crystal structures. *Acta Crystallogr D Biol Crystallogr* **67**, 355-367 (2011).

102. Duan Y, *et al.* A point-charge force field for molecular mechanics simulations of proteins based on condensed-phase quantum mechanical calculations. *J Comput Chem* **24**, 1999-2012 (2003).

103. Whitford PC, Jiang W, Serwer P. Simulations of Phage T7 Capsid Expansion Reveal the Role of Molecular Sterics on Dynamics. *Viruses* **12**, (2020).

104. Noel JK, Whitford PC, Onuchic JN. The shadow map: a general contact definition for capturing the dynamics of biomolecular folding and function. *J Phys Chem B* **116**, 8692-8702 (2012).

105. Levi M, Walak K, Wang A, Mohanty U, Whitford PC. A steric gate controls P/E hybrid-state formation of tRNA on the ribosome. *Nat Commun* **11**, 5706 (2020).

106. Nguyen K, Whitford PC. Steric interactions lead to collective tilting motion in the ribosome during mRNA-tRNA translocation. *Nat Commun* **7**, 10586 (2016).

107. Chan HS, Zhang Z, Wallin S, Liu Z. Cooperativity, local-nonlocal coupling, and nonnative interactions: principles of protein folding from coarse-grained models. *Annu Rev Phys Chem* **62**, 301-326 (2011).

108. Levi M, Noel JK, Whitford PC. Studying ribosome dynamics with simplified models. *Methods* **162-163**, 128-140 (2019).

109. Hess B, Kutzner C, van der Spoel D, Lindahl E. GROMACS 4: Algorithms for Highly Efficient, Load-Balanced, and Scalable Molecular Simulation. *J Chem Theory Comput* **4**, 435-447 (2008).

110. Lindahl E, Hess B, van der Spoel D. GROMACS 3.0: a package for molecular simulation and trajectory analysis. *Journal of Molecular Modeling* **7**, 306-317 (2001).

111. Jackson J, Nguyen K, Whitford PC. Exploring the balance between folding and functional dynamics in proteins and RNA. *Int J Mol Sci* **16**, 6868-6889 (2015).

112. Yang H, Bandarkar P, Horne R, Leite VBP, Chahine J, Whitford PC. Diffusion of tRNA inside the ribosome is position-dependent. *J Chem Phys* **151**, 085102 (2019).

113. Russell RB, Barton GJ. Multiple protein sequence alignment from tertiary structure comparison: assignment of global and residue confidence levels. *Proteins* **14**, 309-323 (1992).

114. Pettersen EF*, et al.* UCSF ChimeraX: Structure visualization for researchers, educators, and developers. *Protein Sci* **30**, 70-82 (2021).

115. Humphrey W, Dalke A, Schulten K. VMD: visual molecular dynamics. *J Mol Graph* **14**, 33-38, 27-38 (1996).

Data availability statement

The atomic coordinates were deposited in the RCSB Protein Data Bank, and EM maps have been deposited in the Electron Microscopy Data bank under accession numbers: 7QI4 and EMD-13980 (consensus monosome), 7QI5 and EMD-13981(classical state), 7QI6 and EMD-13982 (hybrid state).

The atomic coordinates that were used in this study: 3U4M (uL1 from *T. thermophilus*), 4V51 (*T. thermophilus* ribosome with mRNA, tRNA), 4V9D (*E. coli* ribosome), 4Y4P (*T. thermophilus* ribosome with A-, P-, E-site tRNAs), 6QNR (*T. thermophilus* ribosome with experimentally assigned K^+ ions) 6RW4 (mtSSU with mtIF3), 6ZM5 (mitoribosome from actinonin-treated cells) 6ZSG (mitoribosome with mRNA, tRNA), 6ZTJ (*E.coli* expressome), 6ZTN (*E.coli* expressome), 7K00 (*E. coli* ribosome at 2 Å resolution).

Acknowledgments

We thank the EMBO Young Investigator Program, the Northeastern University Discovery cluster and Northeastern University Research Computing staff. Swedish Foundation for Strategic Research (FFL15:0325), Ragnar Söderberg Foundation (M44/16), European Research Council (ERC-2018-StG-805230), Knut and Alice Wallenberg Foundation (2018.0080), Japan Science and Technology Agency (19198049), NIH-R35 grant (GM118141 to A.B.), and MDA Research Grant (MDA-381828 to A.B.). V.S. is supported by the Horizon 2020 - Marie Sklodowska-Curie Innovative Training Network (721757). Y.I. was supported by H2020-MSCA-IF-2017 (799399-Itohribo). The SciLifeLab cryo-EM facility is funded by the Knut and Alice Wallenberg, Family Erling Persson, and Kempe foundations. P.C.W. was supported by NSF grant MCB-1915843. Work at the Center for Theoretical Biological Physics was also supported by the NSF (Grant PHY-2019745). We would like to thank AMD for the donation of critical hardware and support resources from its HPC Fund that made this work possible.

Author contributions

V.S., Y.I., S.A., and J.A. collected cryo-EM data. V.S. and Y.I. processed the data and built the models. V.S., Y.I., R.K.F., A.N., S.A. and A.A. carried out structural analysis. Y.N., K.I. and M.T. performed mass-spec characterization. S.L.D. and A.B. performed biochemical characterization. A.H. and P.C.W. performed molecular simulations. All authors contributed to data interpretation and manuscript writing.

Competing Interests Statement

The authors declare no competing interests.